Nanoscale Horizons

ROYAL SOCIETY OF CHEMISTRY

REVIEW

View Article Online
View Journal | View Issue



Cite this: *Nanoscale Horiz.*, 2022, 7, 112

# Two-dimensional material-based functional aerogels for treating hazards in the environment: synthesis, functional tailoring, applications, and sustainability analysis

Hao Kong,[a] Yun Chen,[a] Guozheng Yang,[a] Bin Liu,[a] Lei Guo,[b] Yan Wang,*[a] Xin Zhou*[a] and Gang Wei *[a]

Environmental pollution is a global problem that endangers human health and ecological balance. As a new type of functional material, two-dimensional material (2DM)-based aerogel is one of the most promising candidates for pollutant detection and environmental remediation. The porous, network-like, interconnected three-dimensional (3D) structure of 2DM-based aerogels can not only preserve the characteristics of the original 2DMs, but also bring many distinct physical and chemical properties to offer abundant active sites for adsorbing and combining pollutants, thereby facilitating highly efficient monitoring and treatment of hazardous pollutants. In this review, the synthesis methods of 2DM aerogels and their broad environmental applications, including various sensors, adsorbents, and photocatalysts for the detection and treatment of pollutants, are summarized and discussed. In addition, the sustainability of 2DM aerogels compared to other water purification materials, such as activated carbon, 2DMs, and other aerogels are analyzed by the Sustainability Footprint method. According to the characteristics of different 2DMs, special focuses and perspectives are given on the adsorption properties of graphene, MXene, and boron nitride aerogels, as well as the sensing and photocatalytic properties of transition metal dichalcogenide/oxide and carbon nitride aerogels. This comprehensive work introduces the synthesis, modification, and functional tailoring strategies of different 2DM aerogels, as well as their unique characteristics of adsorption, photocatalysis, and recovery, which will be useful for the readers in various fields of materials science, nanotechnology, environmental science, bioanalysis, and others.

Received 2nd December 2021,
Accepted 13th January 2022

DOI: 10.1039/d1nh00633a

rsc.li/nanoscale-horizons



## 1. Introduction

The environmental pollution caused by the development of increasing industrialization and frequent human activities, especially toxic gases and particles in air, as well as heavy metal ions and organic pollutants in water, threatened the ecosystem and human health seriously, which has become a global problem that should be faced currently.[1,2] Therefore, it is urgent to develop green, facile, and efficient techniques to monitor and dispose of these pollutants.

Two-dimensional materials (2DMs) such as graphene, transition metal dichalcogenide/transition metal oxide (TMD/TMO), MXene, carbon nitride (CN), and boron nitride (BN) have attracted great attention recently in environmental science due to their excellent physical and chemical properties.[3,4] Among them, graphene has shown high potential on the applications for the adsorption and electrochemical detection of pollutants because of its high mechanical strength, large surface area, and high electrical conductivity.[5] Most 2DMs, including graphene, have large specific surface areas, which are better able to decorate other functional materials. As potential semiconductor materials with proper band gap, TMD/TMO, BP, and CN have strong sensing and photocatalytic properties, which promoted their applications for the electrochemical detection and photocatalytic degradation of pollutants.[6,7] As a new type of 2DMs, MXene also reveals high potential in environmental science owing to its layered structure and a variety of interfacial chemical properties.[8] BN has high specific surface area, good compressibility, and adjustable pore structure.[9] In addition, BN is easy to collect and reuse, showing great potential as a precursor material for the synthesis of adsorbents. However, 2DMs have some defects for the treatment of pollutants, such as easy stacking of

[a] College of Chemistry and Chemical Engineering, Qingdao University, 266071 Qingdao, P. R. China. E-mail: yanwang@qdu.edu.cn, zhouxin@qdu.edu.cn, weigroup@qdu.edu.cn; Tel: +86-15066242101
[b] Institute of Biomedical Engineering, College of Life Science, Qingdao University, 266071 Qingdao, P. R. China

graphene,[10] poor adsorption ability of TMD/TMO and CN,[11] high hydrophilicity of MXene that is not conducive to oil–water separation,[12] difficulty on forming of BN,[13] and others.

The design and fabrication of three-dimensional (3D) aerogels from 2DMs is a facile strategy to overcome the defects of 2DMs in the environmental community. Compared with the lamellar structure of 2DMs, 3D aerogel not only maintains the original excellent properties of 2DMs, but also has some improved features, including higher porosity, specific surface area, mechanical strength and structural stability.[14] 2DM aerogels with high adsorption capacity and abundant binding sites meet the basic needs for environmental detection and remediation applications.[15] For electrochemical sensing applications, 2DM aerogels have excellent electronic conductivity and abundant molecular binding vacancies. For adsorption applications, 2DM aerogels with high porosity and specific surface area and 3D porous structure have high adsorption capacity. The tunable surface hydrophilicity and hydrophobicity makes 2DM aerogels adaptable to various environments, and the 2DM aerogels with high elasticity and mechanical strength have excellent recycling performance. For photocatalytic applications, the 3D interconnected network structure of 2DM aerogels can provide multidimensional electron transport channels, thereby enhancing the separation efficiency of photogenerated charge carriers.

Former researchers have carried out a large amount of excellent work on the design and synthesis of various 2DM-based aerogels. Scheme 1 shows a timeline of important breakthroughs in a typical 2DM aerogels. Since the 2010s, the advent of various 2DM aerogels shows that 2DM aerogels have attracted the attention and research of scientists around the world. In general, the synthesis process of most aerogels can be divided into two processes, *i.e.*, the gelation and drying. Commonly used gelation methods include the sol–gel synthesis,[16] hydrothermal/solvothermal synthesis,[17,18] self-assembly,[19] and 3D printing.[20] The ice template method can be used to control the microscopic pore structure of aerogels before the drying process.[21] In addition, the modifiable surface of aerogels makes it possible to add metals and their oxides/sulfides,[22–24] functional carbon nanomaterials,[25] polymers,[26] and biological materials,[27] endowing new physical and chemical properties to 2DM-based aerogels.

At present, some excellent reviews on the synthesis, modification, and environmental applications of 2DM-based aerogels have been released. Most majority of them, unfortunately, focus on the synthesis and environmental applications of 3D graphene aerogels, while the summary of other 2DMs has rarely been reported. For example, an overview by Lu *et al.* focuses on the design and manufacture of graphene aerogels with various morphologies and structures for the application of photocatalytic degradation to pollutants.[28] In addition, there are some reviews that focused on the synthesis and environmental applications of 3D graphene materials rather than materials limited to the boundaries of aerogels.[29–35] Lee and colleagues emphatically summarized the adsorption application of 3D graphene materials and the role of the ice template method in the design and regulation of 3D graphene materials.[35] By studying these literatures, we realized that it is necessary to carry out a more representative work in this important research field, so as to broaden the research topics.

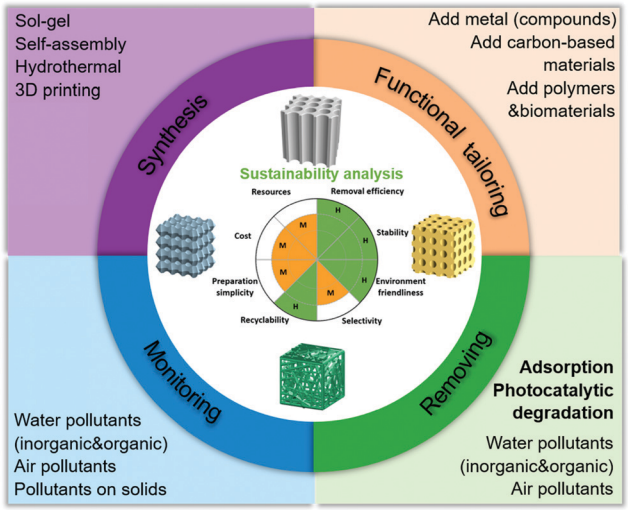


Scheme 2 Schematic presentation of synthesis, functional tailoring, and environmental applications of 2DM-based aerogels.

As shown in Scheme 2, the purposes of this review are to systematically introduce the synthesis and functional tailoring methods of 2DM-based aerogels and their application in the environment. We introduce the synthesis methods of 2DM aerogels in detail (including sol–gel method, self-assembly method, hydrothermal method, 3D printing) and functional tailoring methods (including the addition of metals, carbon functional materials, polymers and biomaterials). In addition, we demonstrate the family of novel multifunctional 2DM-based aerogels, including graphene, TMD/TMO, CN, BN, MXene, and others. The application of 2DM aerogel in the field of environmental monitoring and remediation (adsorption and photocatalysis) for various organic and inorganic pollutants in water


Scheme 1 Timeline of important breakthroughs for 2DM aerogels.

and air is presented and discussed. Finally, the sustainability of 2DM-based aerogels in environmental applications and their future prospects and challenges are discussed. We believe that this comprehensive review will be valuable for readers to understand the functions and properties of 2DM-based aerogel materials, and to promote the design and fabrication of structure- and function-tailorable aerogels for energy storage, environmental science, analytical science, and biomedical applications.

## 2. Synthesis of 2DM-based aerogels

There are several methods that can be utilized to synthesize 2DM-based aerogels, including the sol–gel method, hydrothermal method, self-assembly method, 3D printing method, and others. Among them, the driving force for the formation of 3D network structure is mainly covalent (chemical binding) and noncovalent interactions(hydrogen bonding, coordination, electrostatic interaction, and π–π stacking).[36] In this section, we will introduce some typical examples and summarize the synthesis methods and characteristics of 2DM-based aerogels.

### 2.1. Sol–gel synthesis

Sol–gel synthesis is a traditional wet chemical method for preparing 2DM-based aerogels.[37] The processing temperature of the sol–gel synthesis is low, and the reaction is easy to control, making it possible to precisely control of the synthesis process and achieve desired microstructure of the gels. The process of preparing gels by traditional sol–gel method roughly includes three key steps: sol–gel reaction, aging, and drying. In this part, we will demonstrate the sol–gel synthesis and drying technologies of 2DM aerogels. Drying technology is also applicable to other synthesis methods and will not be introduced in the following part.

Traditional organic sol–gel method is an original method to prepare graphene aerogels. Worsley *et al.* reported the preparation of graphene aerogel using the resorcinol-formaldehyde (RF) sol–gel chemical method for the first time.[37] As shown in Fig. 1a, in this typical reaction, the graphene oxide (GO) suspension was uniformly dispersed and then the RF and sodium carbonate catalysts were added. After sealed heating at 85 °C, GO was combined with RF to form GO-RF hydrogel through the sol–gel conversion, in which acetone was used to replace the water in the original hydrogel. The subsequent supercritical $CO_2$ drying step converts GO-RF hydrogel into

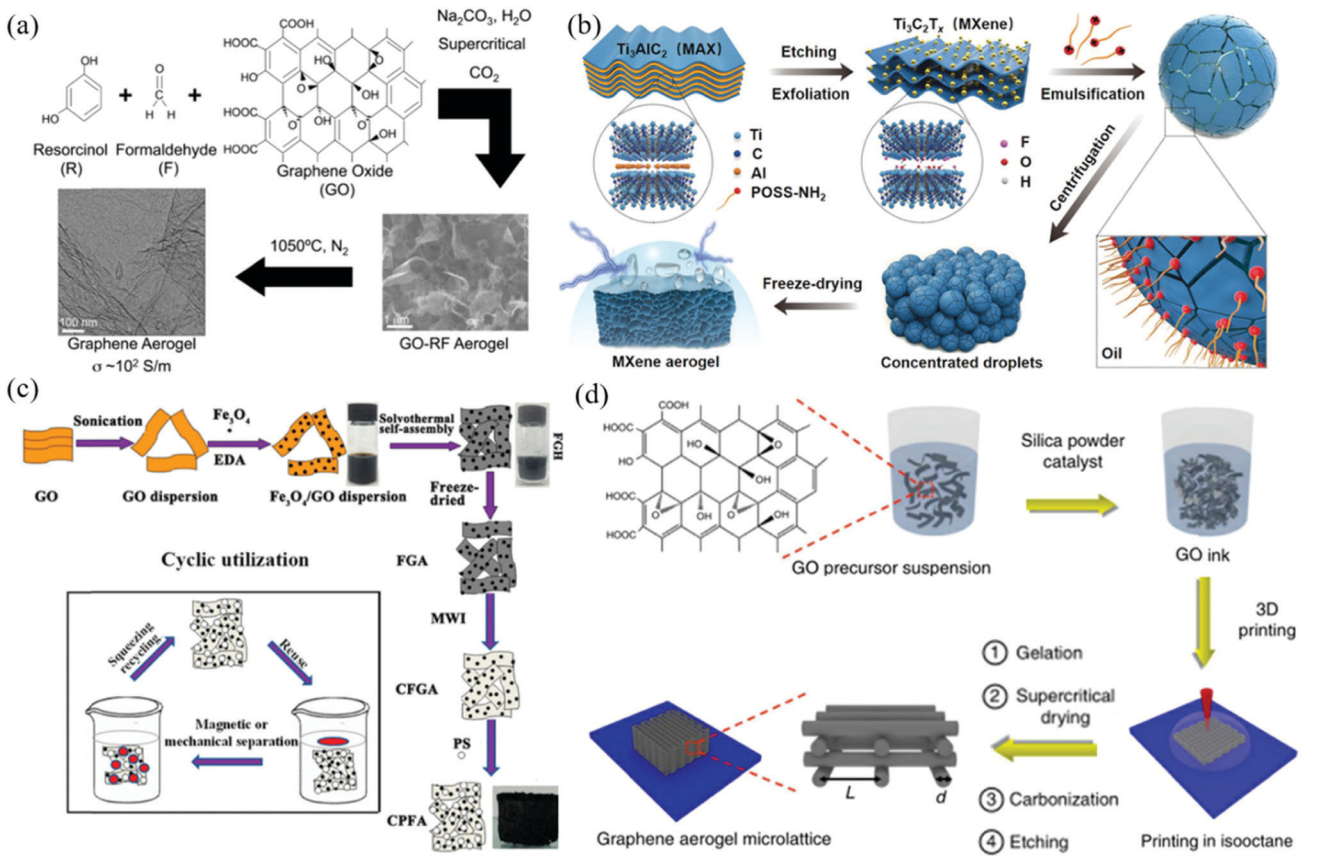


Fig. 1 Synthesis strategies of 2DM-based aerogels: (a) Preparation schematic diagram of graphene aerogel.[37] Copyright 2010, American Chemical Society. (b) Schematic diagram of MXene aerogel constructed with MXene surfactant.[46] Copyright 2019, Wiley-VCH. (c) Preparation process diagram of CPFA.[18] Copyright 2015, American Chemical Society. (d) 3D print schematic diagram of the manufacturing process of graphene aerogel.[51] Copyright 2015, Nature Publishing Group.

 

aerogel, which was further pyrolyzed to form graphene aerogel (GA) at 1050 °C. The carbonatized RF polymer was mixed with reduced graphene oxide (RGO) to form a hybrid RGO/carbon aerogel during the pyrolysis.

Furthermore, the Qu group developed a surfactant-foaming sol–gel method for the synthesis of graphene aerogels, in which GO-liquid crystals (LCs) were effectively reconstructed using the microbubbles as templates and large graphene hydrogel blocks (GHB) were synthesized.[38] After simple freezing and air drying, graphene aerogels with complete structure, size of about 1 $m^2$, super-elasticity (up to 99% compression strain), and ultra-low density (2.8 mg $cm^{-3}$) were obtained. The whole synthesis process was very simple, green, and economical, and could be used for mass production of large graphene aerogel blocks. It was suitable to be used as high compression force absorbers, solar thermal management materials, and ultra-light refractories, presenting very broad application prospects.

Traditional sol–gel synthesis uses molecular precursors such as organic alkoxides or chlorides. For many 2DMs, it is hard to find corresponding precursor to form gel, which limits the application of the sol–gel method in the preparation of 2DM aerogels. In addition, the resulting aerogels are usually amorphous, and the crystallization requires further high temperature treatment, which requires high energy consumption and cost.

In conventional drying process, the liquid surface tension of the solid–liquid vapor interface of the hydrogel produces capillary stress in the capillary wall, which leads to the collapse of macrostructure and the shrinkage of the aerogel. In order to reduce the damage of the capillary stress to the gel network, some solvents with low surface tension (such as ethanol, ethyl ketone and acetone) are often used to replace the water in the hydrogels. At the same time, it is necessary to choose a suitable drying method to avoid the capillary stress. For instance, the freeze-drying, supercritical drying, and atmospheric drying are commonly used to dry the hydrogels to prepare strong, porous, and lightweight aerogels.

In the process of supercritical drying, the pressure and temperature of the closed pressure vessel exceed the critical point of the solvent, and the solvent changes from liquid phase to supercritical fluid between gas and liquid. In the supercritical state, there is no gas–liquid interface, so there is no capillary stress.[39] The commonly used supercritical fluids are $CO_2$, ethanol, acetone, and many others.

The supercritical drying process usually requires high tightness and high cost of autoclave, while the atmospheric drying provides the possibility for large-scale industrial production of 2DM-based aerogels because of its simplicity, green synthesis, and low energy consumption. However, the atmospheric drying will destroy the gel network, hence it is necessary to have a strong gel structure or use a solvent with low surface tension to replace the solvent for the gel. Yan *et al.* synthesized macroporous graphene hydrogels by the self-assembly and with hydrazine hydrate as the reducing agent.[40] After pre-freezing treatment, the obtained hydrogel can be naturally dried into graphene aerogel without obvious volume shrinkage ($<5\%$) or cracks. According to the Laplace formula,[41] when the stiffness of the aerogel is similar to the compression modulus, the volume shrinkage of the graphene aerogel can be effectively hindered by expanding the pore radius, reducing the solvent surface tension or increasing the contact angle. The synthesized graphene aerogels are strong enough to resist the capillary stress caused by solvent evaporation, hence there is no obvious volume shrinkage.

Because of its simple operation and low cost, the freeze-drying is the most commonly used drying method for the synthesis of 2DM-based aerogels. According to the principle that the boiling point decreases with the decrease of the pressure, the freeze drying method reduces the pressure below the three-phase point pressure, and the water in the hydrogel can be sublimated directly from the solid state to the gaseous state without going through the liquid state, thus limiting the capillary stress and retaining the solid 3D porous network of the hydrogel.

Generally speaking, the samples that put into the dryer have to be pre-frozen in advance, and the freezing before that also has a certain effect on the pore structure of the aerogel. The ice template method (also known as freeze casting) is often used to regulate the gel network structure before freeze-drying. The ice template method means that the solvent in the suspension of 2DM solidifies to produce ice crystals in the pre-freezing process, and the ice crystals become the growth template of nanomaterials in the suspension, which plays a limiting role. After freeze drying, the ice crystals are sublimated from the solid phase to the gas phase, the template is removed, and the structure formed by the nanomaterials is retained.

Zhan *et al.* used the freeze-drying method to creatively add one-dimensional (1D) polydopamine (PDA)-functionalized multi-walled carbon nanotubes (MWCNT-PDA) to 3D graphene framework to synthesize solid graphene/MWCNT-PDA composite aerogels (GCPCA).[42] Before freeze-drying, the hydrogel was dialyzed with deionized water and ethanol, and after dialysis, the hydrogel was gradually pre-frozen at −20, −50, and −80 °C, respectively. The obtained results showed that the average size of aerogel micropores decreases with the decrease of pre-freezing temperature. Interestingly, when the pre-freezing temperature dropped to −80 °C, the tiny ice crystals around the edge of the aerogel formed rapidly, while the ice crystals in the core formed slowly. Therefore, due to the differences in growth rate and size of ice crystals inside and outside, aerogels with unique pore size orientation were produced, showing an interesting ''cabbage-like'' graded porous structure. The directional arrangement of the ''cabbage-like'' graded porous structure greatly increases the flow of liquid in the pores, thus giving the aerogel super absorptive capacity to deal with the pollutants.

Directional freezing method is a kind of ice template method, which uses the anisotropy of solvents in the temperature field to control the orientation of the gel network, and then controls the structure and morphology of the final aerogel by regulating the growth and structure of ice crystals during freezing. Yang *et al.* imitated the stem of Thalia dealbata with natural 3D interconnected layered structure by using

bi-directional freezing technology and freeze-drying method to synthesize graphene aerogel with extraordinary mechanical strength and elasticity.[21] Bi-directional freezing was achieved by pouring the precursor suspension into a polydimethylsiloxane (PDMS) wedge with a certain tilt angle, which produced both horizontal and vertical temperature gradients during freezing. In the subsequent process, the ice crystals were sublimated and reduced by thermal annealing to form a template of biomimetic graphene aerogel similar to the hierarchical structure of plant stems. The nucleation and growth of ice crystals as well as the final microstructure, porosity, and orientation of aerogels could be adjusted by changing the concentration of suspension, the tilt angle of PDMS wedge and the cooling rate.

### 2.2. Self-assembly synthesis

Self-assembly is a common approach for synthesizing 2DM-based aerogels. Different from traditional sol–gel method, the self-assembly method will no longer be restricted by the precursors. In addition to graphene, other 2DM aerogels have also been widely developed. With the participation of cross-linking agent, the layers of 2DMs are combined by electrostatic interaction, hydrogen bond, and π–π interaction.

Luo *et al.* synthesized graphene hydrogels with high adsorption capacity by chemical reduction-induced GO self-assembly, using tannic acid as reducing agent and physical cross-linking center.[43] The synthesis method has the advantages of mild conditions, simple operation, and low cost, which makes it possible to produce highly efficient adsorbents for water purification on a large scale. In addition, 2DMs can be assembled into aerogels by γ-ray irradiation. He and co-workers synthesized a kind of GA with honeycomb porous structure by a simple γ-ray irradiation-induced reduction, self-assembly, and freeze-drying process.[44] Under γ-ray irradiation, water molecules can be decomposed into oxidized state ($^{\bullet}OH$) and reduced state ($H^{\bullet}$ and $e_{aq}^{-}$). The oxidized free radicals in water are scavenged by isopropanol free radical scavengers and converted into reductive free radicals, which can reduce GO and induce its self-assembly into 3D gels. In another case, Xu *et al.* reported a simple one-pot freeze-drying-induced self-assembly method that combined with *in situ* thermal decomposition–reduction to construct a 3D porous $MoS_2$/graphene sheets (GS) hybrid aerogel by loading $MoS_2$ onto graphene skeleton.[45] The self-assembly process occurs between Mo precursor and GO under the influence of electrostatic interaction, and then formed $MoO_3$ reacted with the decomposed $H_2S$ to create $MoS_2$. Meanwhile, GO was reduced by $H_2S$ to GS in this reduction process simultaneously. The obtained aerogel has highly interconnected network structure and good structural stability. This manufacturing method is easy to expand the scale and has a broad prospect in practical application.

As shown in Fig. 1b, Shi *et al.* synthesized MXene-based nanoparticles (NPs) using MXene–$Ti_3C_2T_x$ and oil-soluble amino polyhedral oligomeric silsesquioxane (POSS–$NH_2$) as templates, named as MXene-surfactants (MXSs).[46] $Ti_3C_2T_x$ and POSS–$NH_2$ self-assembled at the interface between two incompatible liquids of water and oil, forming overlapping MXene nanosheets. After stacking, solid-like components with excellent mechanical properties were produced. The structured Pickering emulsion made from MXSs was freeze-dried to prepare light hydrophobic MXene aerogel, which exhibited potential application for oil absorption and electromagnetic interference shielding. In another study, Wang and co-workers developed a simple method based on self-assembly to prepare self-supporting CN aerogels without using any organic/inorganic cross-linking agents.[47] Firstly, CN nanosheets were self-assembled and gelated in sol solution to form CN hydrogel, and CN aerogel was obtained after conventional freeze-drying. The aerogels have large specific surface area, rich functional groups and 3D network structure, and exhibit high photocatalytic activity for hydrogen evolution and $H_2O_2$ production under visible light irradiation.

### 2.3. Hydrothermal/solvothermal synthesis

Hydrothermal method is the most common wet chemical approach for the synthesis of 2DM-based aerogels. It refers to a method of preparing materials under the condition of high temperature and high pressure in an airtight pressure vessel with water as solvent, where the speed of gelation can be not only improved, but also ensure the integrity of the gel.

Kim and colleagues reported a $MoS_2$/graphene aerogel (MGA) prepared by one-pot hydrothermal method for electrochemical detection of $H_2O_2$ and glucose.[48] The porous network structure of MGA provides vacancies for enzyme immobilization, and the high conductivity of MGA increases the electron conduction rate of the detector. The electrochemical biosensor prepared by MGA was sensitive, rapid, and specific for the detection of $H_2O_2$ and glucose. In another case, Zhang *et al.* synthesized cellulose nanofiber/graphene aerogel (CGA) by a simple and environmentally friendly method, including hydrothermal self-assembly, freeze-drying, and carbonization.[49] In the hydrothermal process, ethylenediamine was selected as the dopant to promote the cross-linking of GO to form highly porous 3D nanostructures. The as-synthesized CGA exhibited good electrochemical performance and adsorption performance, which could be used as materials for the fabrication of high-performance supercapacitors and adsorbents.

Solvothermal method is a development of hydrothermal method, and the difference is that it uses organic solvent rather than water. As shown in Fig. 1c, Zhou *et al.* prepared a hydrophobic and magnetic polystyrene/$Fe_3O_4$/graphene aerogel composite (CPFA) by solvothermal reaction of GO with $Fe_3O_4$ and polystyrene (PS) inethylene glycol.[18] In the graphene aerogel framework, $Fe_3O_4$ NPs and PS microspheres were uniformly distributed on the 3D gel network structure. In the solvothermal process, the mixed solution was sealed in a polytetrafluoroethylene lined stainless steel autoclave and the self-assembly occurred under the condition of high temperature and high pressure. The hydrogel was freeze-dried and converted into aerogels. After microwave irradiation in $N_2$ environment, the excess oxygen-containing groups were removed and the compressibility was obtained. $Fe_3O_4$ not only provides magnetism in the system, but also enhances the cross-linking between

 

graphene sheets and improves the hydrophobicity and compressibility of graphene aerogel composites, presenting adsorption and recoverability for oil adsorption applications.

### 2.4. 3D printing synthesis

3D printing technology is an advanced technique for the synthesis of 2DM-based aerogels.[50] It realizes the formation of gel network by printing rather than gelation or self-assembly. Direct ink writing (DIW) is a 3D printing method based on extrusion, which has become a promising technology for manufacturing 2DM aerogels. As shown in Fig. 1d, Worsley and coworkers reported a periodic graphene aerogel microlattice prepared by 3D printing.[51] However, there are two key problems in the 3D printed graphene aerogels. The first problem is how to adjust the GO precursor suspension to make it to printable ink, and the second problem is how to set up the 3D printing process to ensure that the printing structure is moist. By increasing the concentration of GO to 40 mg $ml^{-1}$ and adding tackifier silica filler, the viscosity of GO suspension was improved, and the first problem was solved. The second problem was solved by printing in a bath of an organic solvent (isooctane) that is incompatible with ink. The 3D printed graphene aerogel has low density, high electrical conductivity, super compressibility, and ultra-high Young's modulus.

Zhang *et al.* combined multi-nozzle on-demand inkjet with freeze casting to print GA with directional and boundless microstructure.[52] In particular, this 3D printing process can quickly freeze water-based GO suspensions and selectively solidify water droplets into ice crystals on cold water tanks (−25 °C) well below the freezing point of water. The graphene aerogel has pure, continuous, borderless, controllable microstructure, and real 3D structure. In another study, Fan and colleagues developed a DIW 3D printing method for programmable construction of patterned hybrid CN aerogel films.[20] g-$C_3N_4$ nanosheets were used as the building blocks and sodium alginate (SA) was added to increase the viscosity of the ink. At the same time, three printing approaches were shown, including printing directly in the air and printing in a support library composed of $CaCl_2$/glycerol solution or Pluronic F127 to achieve the versatility of printing. The printed Au-g-$C_3N_4$-SA hybrid aerogels exhibited excellent photocatalytic properties.

## 3. Family of 2DM aerogels

The 2DM family contains many members, but not all 2DMs can be made into 3D aerogels. Some 2DMs can independently support the aerogel network, while many 2DMs can only form aerogels with the help of the skeleton of other substances. In this section, we will summarize and outline different types of aerogels using 2DMs, such as graphene, TMD/TMO/TMP, CN, MXene, BN, and many others.

### 3.1. Graphene aerogels

Graphene, as an allotrope of carbon, has a regular hexagonal honeycomb 2D structure. Carbon atoms are connected to each other through a unique electron cloud.[39,53] Graphene has good planar conductivity and high Young's modulus, and its electrical conductivity and thermal conductivity are higher than those of other known 2DMs.

Xu *et al.* for the first time combined the spinning technology with the ice template freezing strategy to prepare GO aerogel fibers with "porous core-dense shell" structure from layered ordered GO liquid crystals. The electrical conductivity of the aerogels was increased by chemical reduction and thermal annealing.[54] In this porous core–shell structure, graphene sheets are densely piled on the shell surface to form a wrinkled surface, and graphene sheets are connected with each other in the shell and arranged along the fiber axis to form a porous structure. This structure greatly enhanced the mechanical strength and toughness of RGO fiber, which was perfectly integrated with electrical properties, and revealed a good application potential of conductive light porous materials. Hong *et al.* introduced fluorinated groups into graphite seeds by one-step solution impregnation method to prepare 3D graphene aerogels with hydrophobic surface and good mechanical stability, which showed excellent adsorption properties for oil and organic solvents and with good recyclability (Fig. 2a).[55] In addition, taking advantage of the high conductivity and large specific surface area of graphene sheets, Fu *et al.* prepared graphene aerogels loaded with Ni/MnO particles as bifunctional oxygen catalysts.[56] A large number of particle anchoring sites were provided by the surface of graphene, so that Ni and MnO were uniformly dispersed in the prepared graphene aerogels, which synergistically enhanced the bifunctional electrocatalytic performance of Ni–MnO/RGO catalyst for oxygen reduction reaction (ORR) and oxygen evolution reaction (OER). In another case, Huangfu *et al.* used graphene as carrier to load $Fe_3O_4$ NPs for the formation of hybrid graphene aerogels, which exhibited enhanced electromagnetic shielding effects.[57]

### 3.2. TMD/TMO/TMP aerogels

TMD is a layered 2D semiconductor material, which is widely used in the fields of electrochemical sensing, supercapacitors, and photocatalysis because of its unique physical and electrochemical properties.[58] Crane *et al.* used rapid RF sol–gel chemistry to wrap TMD sheets in carbon aerogel matrix to prepare TMD-doped carbon aerogel composites.[59] $MoS_2$ aerogel has significantly improved the charge transfer resistance and magnification ability, and $WS_2$ aerogel also shows excellent cycle stability. This method provided a possibility for the rapid synthesis of carbon aerogel composites for all stable TMDs. Yang *et al.* reported a carbon/tin sulfide aerogel (SSC@$SnS_2$) with "skeleton/skin" morphology.[60] $SnS_2$ nanosheets were wrapped on the CNF/GO skeleton as thin skins, and they provided abundant active sites for storing sodium ions, while the conductive CNF/GO skeleton promoted the rapid transfer of electrons. The composite aerogel exhibited excellent electrochemical performance, which makes it possible to develop high performance sodium ion battery materials in the future. In another case, Zhang *et al.* reported a $MoSe_2$–$CoSe_2$/NGA composite aerogel grown on N-doped graphene aerogel (NGA)

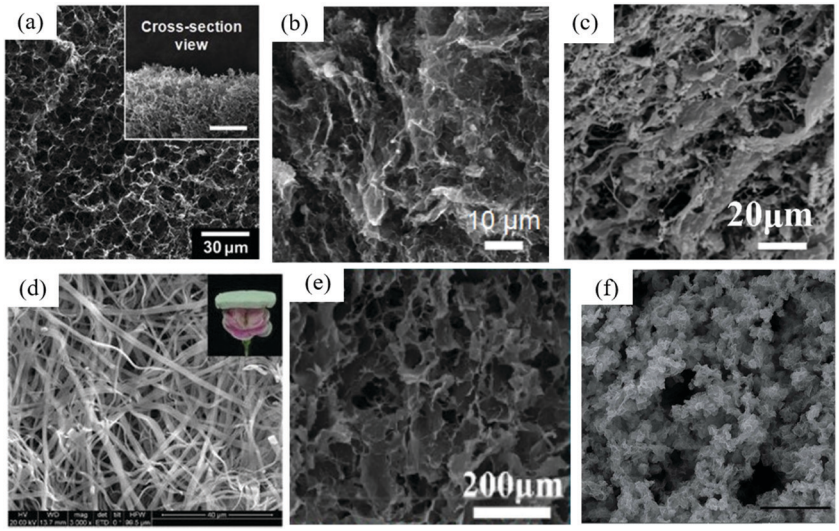


Fig. 2 Typical SEM images of 2DM aerogels: (a) GO aerogel.[55] Copyright 2015, Elsevier. (b) B-$TiO_{2-x}$/G aerogels.[64] Copyright 2019, Springer. (c) g-$C_3N_4$ hybrid aerogel.[69] Copyright 2019, Elsevier. (d) BN aerogel.[75] Copyright 2019, Wiley-VCH. (e) MXene/ANFs aerogel.[78] Copyright 2020, American Chemical Society. (f) Palladium aerogel.[84] Copyright 2017, Royal Society of Chemistry.



with $MoSe_2$–$CoSe_2$ nanosheets.[61] NGA provided a stable conductive network because of its high specific surface area, and $MoSe_2$–$CoSe_2$ nanosheets provided sufficient specific capacity because of its high accessibility and multiple redox properties. Therefore, the $MoSe_2$–$CoSe_2$/NGA composite aerogel served as a stable system for lithium diffusion and electron transport, and was an ideal electrode material for lithium battery.

In recent years, 2D TMO materials have attracted more and more attention because of their excellent electrical, optical, chemical, and thermal stability, as well as abundant active sites.[62] For example, Zhang *et al.* synthesized MNSs@d-$Ti_3C_2$ aerogels by loading 2D $MnO_2$ nanosheets (MNSs) on delaminated-$Ti_3C_2$ skeletons through electrostatic self-assembly.[63] The composite aerogels made of two kinds of 2D materials gave full play to the electrical conductivity of d-$Ti_3C_2$ and the polarity of MNSs, and their excellent synergistic effects provided aerogels with high specific surface area and macroporous structure. These excellent properties make the composite aerogel MNSs@d-$Ti_3C_2$ a good sulfur fixing agent in lithium-sulfur battery. Zhu *et al.* used one-pot hydrothermal method to assemble graphene nanosheets and anoxic black $TiO_{2-x}$ nanosheets into 3D interconnected B-$TiO_{2-x}$/G aerogels (Fig. 2b).[64] Compared with $TiO_2$, the narrow band gap anoxic $TiO_{2-x}$ with $Ti^{3+}$ has better electrical conductivity. Thanks to the excellent synergistic effects of oxygen vacancy and conductive carbon matrix, the formed B-$TiO_{2-x}$/G aerogel was regarded as an ideal anode material for lithium–ion capacitors due to its high electrical conductivity, abundant active centers, and short ion diffusion pathway. In another case, Zhou *et al.* synthesized dense packed $Sb_2O_3$ nanosheets–graphene aerogel composites by solvothermal reaction.[65] $Sb_2O_3$ nanosheets grow uniformly on the surface of GO, and multi-layer stacking promotes the formation of aerogel skeleton structure. Thanks to the synergistic effect of $Sb_2O_3$ nanosheet and graphene nanosheet, the composite aerogel has excellent electrochemical performance and is an ideal anode material for sodium ion battery.

Transition metal phosphide (TMP) has an ultra-thin 2D structure, which can provide abundant active sites and promote mass/charge transfer, so it is regarded as a high-performance electrocatalyst comparable to precious metal catalysts. Yang *et al.* used ice template method to assemble 2D ultrathin CoP nanosheets that derived from alginate into 3D CoP aerogels.[66] The obtained CoP nanosheet aerogel had a highly porous structure to facilitate the mass transfer of hydrogen evolution reaction (HER), and showed remarkable stability and excellent electrocatalytic performance at all pH values. In a further study, they reported a kind of 3D $Ni_5P_4$ aerogel based on 2D ultrathin $Ni_5P_4$ nanosheets derived from alginate.[67] Starting from nickel alginate aerogel, $Ni_5P_4$ nanosheet aerogel was oxidized and phosphated into NiO nanosheet aerogel and $Ni_5P_4$ nanosheet aerogel. The obtained $Ni_5P_4$ nanosheet aerogel exhibited high catalytic activity for the hydrogen evolution.

### 3.3. CN aerogels

CN, as a 2D conjugated polymer, has a broad application prospect in the fields of photocatalysis and electrochemical sensors because of its unique properties. Among them, g-$C_3N_4$ with conjugated polymer network has become a kind of medium band gap semiconductor because of its high physical and chemical stability, unique electronic structure, and optical properties.[68]

Qi *et al.* prepared 3D g-$C_3N_4$ hybrid aerogels with g-$C_3N_4$ as the main scaffold through the cross-linking of carboxymethyl cellulose and β-cyclodextrin.[69] Compared with pure g-$C_3N_4$ aerogels, the formed composite aerogels showed longer-term stability, easier separation, and stronger photocurrent. The composite aerogel has the characteristics of high porosity, large specific surface area, and 3D network structure (Fig. 2c),

 

showing good synergistic effect in photocatalysis application. The removal rate of rhodamine B (RhB) in 90 min can reach 97.99%, and the removal rate remains basically unchanged after 5 cycles. In another study, Pan *et al.* reported a 2D RGO-$NiS_2$ double catalyst modified g-$C_3N_4$ nanosheet aerogel that synthesized by the thermal oxidation, hydrothermal synthesis, and freeze-drying process.[70] Compared with the conventional pure g-$C_3N_4$, the photocatalytic performance of the composite aerogel was improved significantly, which is mainly attributed to the improvement of the overall electrical conductivity of the composite aerogel by the synergistic modification of RGO–$NiS_2$ double co-catalysts. Yang *et al.* reported the synthesis of a fibrous AgNPs/g-$C_3N_4$ aerogel through *in situ* assembly and step-by-step heat treatment.[71] AgNPs not only had plasmon enhanced photocatalytic activity, but also effectively improved the limited absorption of g-$C_3N_4$ and the charge-hole recombination caused by low conductivity. Therefore, the composite aerogel revealed high efficiency for photo-catalyzing pure methanol into hydrogen and formaldehyde at room temperature without producing CO or $CO_2$.

### 3.4. BN aerogels

Hexagonal boron nitride (h-BN) is an excellent layered material with high thermal conductivity and stability. However, BN nanosheets have inherent brittleness limitations, which leads to poor mechanical properties of BN aerogels made from them.[72] In order to solve the problem of poor mechanical properties of BN aerogels, surface modification and mechanical reinforcement could be used. For example, Zhu *et al.* used the ice template method to synthesize a flame-retardant and heat-insulating aerogel combining glutamine-grafted BN nanosheets (BNNSs-g) and CNFs. The surface modification of glutamine and the addition of CNFs improved the mechanical strength of the composite aerogel. The ice template method not only promoted the directional arrangement of BN nanosheets in the aerogel, but also kept the anisotropy of the thermal conductivity of BN nanosheets. The flame retardancy of the composite aerogel decreased with the increase of the proportion of BNNS, which indicated that BN nanosheets play a key role in the flame retardancy. In another case, Yu *et al.* prepared BN/polyvinyl alcohol (PVA) composite aerogels with high thermal conductivity by the ice template self-assembly and hot pressing.[73] When BN/PVA hydrogel was frozen, BN nanosheets were extruded on the ice crystal interface to form a 3D network, and then freeze-dried to form BN/PVA aerogel. After hot compression, there is a better thermal contact between the BN sheets, thus further improving the thermal conductivity of the aerogel, up to 10.04 $W\ m^{-1}\ K^{-1}$. Different from the BN aerogels with anisotropic thermal conductivity mentioned above, Gu *et al.* developed a new type of BN aerogel with isotropic thermal conductivity.[74] The ice template method promoted the formation of oriented BN walls in aerogels, and xylitol crystals were filled in the micropores of BN aerogels. The perpendicular arrangement of xylitol crystals to the BN wall provided an additional heat transfer pathway, which counteracts the anisotropy of BN aerogels.

In addition, 2D BN nanoribbons can also be used to prepare BN aerogels to solve the problem of poor mechanical properties. Zhang *et al.* reported a kind of 3D BN aerogel formed by winding 2D BN nanoribbons.[75] Melamine (M) and boric acid (B) were assembled by hydrogen bond in hot distilled water/*tert*-butanol co-solvent to form M·2B hydrogel. After freeze-drying and high-temperature $NH_3$ pyrolysis, the aerogel network interwoven with BN nanoribbons was obtained (Fig. 2d). This unique ribbon interweaving structure enables BN aerogels to maintain excellent mechanical properties and flexibility over a wide temperature range of −196 to 1000 °C.

### 3.5. MXene aerogels

MXene is a kind of graphene-like transition metal nitride or carbide material, but since it was discovered in 2011, it has attracted wide attention due to its large specific surface area, electrical conductivity, good biocompatibility, and good mechanical strength.[36] Recently, Chen *et al.* used bacterial cellulose as an adhesive to connect MXene monolayers to form continuous multilayers, thus solving the problem of poor interaction between MXene thin layers and preparing lightweight compressible and elastic carbon aerogels (CECA).[76] CECA-based wearable sensor exhibited high sensitivity and strain, low pressure detection limit, and stable structure. Zhou and colleagues used calcium alginate (CA)SA as a spacer between MXene layers to prevent the reaccumulation of MXene lamellar structure and prepared spongy $Ti_3C_2T_x$/CA ultrathin aerogel films.[77] The spongy structure of $Ti_3C_2T_x$/CA aerogel film was conducive to multiple reflection and scattering absorption of incident electromagnetic waves, so it is a kind of ultra-thin and high performance electromagnetic shielding material.

By combing aramid nanofiber (ANF) with excellent mechanical properties with MXene, Wang *et al.* prepared MXene/ANFs composite aerogel to make up for the shortcomings of poor resilience and easy oxidation of MXene.[78] the formed MXene/ANFs aerogel revealed regular 3D delamination and ''mortar-brick''porous structure (Fig. 2e), which showed excellent compression resilience and sensing properties, presenting great potential to be used as a piezoresistive sensor in human motion detection. Liao *et al.* prepared cobalt sulfide-modified MXene/N-doped carbon foam (CoS@MXene/CF) aerogels by *in situ* growth and annealing.[79] The electrode material made of CoS@MXene/CF aerogel exhibited high specific capacity and could still maintain a high specific capacity after 10 000 cycles.

### 3.6. Other 2DM aerogels

In addition to the above-mentioned 2DMs that can be used to make aerogels, there are also some other 2DMs that can also be used to make aerogels, such as 2D metal–organic frameworks (MOFs), layered double hydroxide (LDH), metal nanosheets, black phosphorus (BP), and so on.

2D MOFs can be formed by designing various metal-containing nodes and organic ligands to control the self-assembly between the metal and the ligand.[80] Zhang and colleagues developed a new route to prepare metal–organic aerogels (MOA).[81] 2D Ni(BDC)(BDC = 1,4-benzenedicarboxylate)

nanosheets are assembled into a preformed gel-like high internal phase emulsion (HIPE) at the oil–water interface of 1 : 1 cyclohexane/water. After supercritical $CO_2$ replacement and freeze-drying, the inner oil phase and outer water phase can be removed to make a hollow spherical MOA that retains the HIPE framework.

LDHs is considered as an ideal 2D inorganic layered material for energy storage due to its interchangeability and wide tunability of metal ions. The composite aerogel made of 2D LDH and other 2DMs can effectively solve the problem of poor electrical conductivity of LDH. For example, Zheng *et al.* hydrothermally integrated MXene, $NiCo_2$-LDHs, and RGO together into a 3D layered aerogel ($NiCo_2$-LDHs@MXene/RGO).[82] The addition of MXene and RGO provides good electrical conductivity for the aerogel as a whole, which makes it possible for $NiCo_2$-LDHs@MXene/RGO aerogel to be used as a high-performance energy storage device. In another case, Xu *et al.* reported a novel 3D hybrid aerogel based on N, S co-doped graphene (N, S-RGO), $WSe_2$ nanosheets, and NiFe-LDH.[83] N, S co-doped RGO and 2D $WSe_2$ nanosheet aerogels synthesized by hydrothermal method were combined with NiFe-LDH nanosheets self-assembled under electrostatic interaction to form the N, S-RGO/$WSe_2$/NiFe-LDH aerogel. Different 2D components, synergism, and versatility played a key role in the realization of efficient energy storage devices.

In the past, the 3D networks of noble metal aerogels are formed by the interconnection of nanochains and the gelation of metal NPs, but the aerogels based on noble metal NPs are difficult to be synthesized due to the lack of internal force. Noroozifar *et al.* reported for the first time the synthesis of palladium (Pd) aerogels through the assembly of Pd nanosheets.[84] In the process of synthesis, CO was used as reducing agent and surface limiting agent to assemble Pd nanosheet hydrogel from the precursor acetylacetone palladium dissolved in glacial acetic acid. After supercritical drying of acetone, Pd aerogel exhibited high specific surface area and high mass current density, which was 5.8 times higher than that of commercial Pd/C catalyst, mainly ascribed to the large surface area brought by nanosheet structure in Pd aerogel (Fig. 2f). In a subsequent study, they further explored the synthesis of Pd aerogels in carboxylic acid solvents with different alkyl groups.[85] Pd aerogels in acetic acid and propionic acid had better morphology and higher catalytic activity because their corresponding alkyl groups methyl and ethyl played the role of mild capping agent.

BP has similar properties to graphene, such as good biocompatibility and excellent photothermal properties. However, due to its easy oxidation and instability, it is difficult to synthesize pure BP-based aerogels. With the support of graphene scaffolds, Zhang and colleagues synthesized GO and BP nanoflakes (BPNF) composite 3D aerogels (GO/BPNF aerogels) for the first time.[86] Under the action of cross-linking agent polyoxypropylene diamine, the aqueous solution of GO and BPNF began to gelate in the dark environment, and the GO/BPNF aerogel was obtained after freeze-drying. In another case, Du *et al.* synthesized CNF/BP hybrid aerogel using cellulose as the framework.[87] The existence of BP nanosheets makes the aerogel as a whole to obtain a good photothermal conversion efficiency (up to 85%) and a certain degree of flame retardancy.

In addition to 2D nanosheets that can be made into aerogels, there are also some aerogels based on 2D nanoribbons. For instance, Wang *et al.* prepared 3D porous vanadium nitride nanoribbon aerogel (PVNNRAs) by hydrothermal method and freeze-drying.[88] The formed 3D porous structure, high specific surface area, and porosity provided abundant electrocatalytic active sites and rapid electron transfer, making the created aerogel a potential electrode material for solar cells.

## 4. Functional tailoring of 2DM aerogels

Both physical and chemical properties of aerogels can be tailored by adjusting the experimental parameters of the synthesis process. The ice template method is a good strategy for the preparation of aerogels with special network structure. Besides, additional functions can be incorporated into the gel network by adding corresponding substances to the aerogels. For example, semiconductor particles can endow aerogels with photocatalytic function,[89] magnetic NPs can make aerogels magnetic,[18] and carbon nanotubes (CNTs) can also be incorporated into aerogels to improve their compressibility, strength, electrical conductivity, and porosity.[42] This part will focus on some methods to regulate the functions of aerogels, including the addition of metals and metal compounds, carbon nanofunctional materials, polymers and biomaterials to improve the functions and properties of fabricated 2DM aerogels.

### 4.1. Addition of metals and metal compounds

Metals and metal compounds such as Ag, Au, ZnO, $TiO_2$, $Fe_2O_3$, CuO, $SnO_2$, $MnO_2$, $Bi_2S_3$, and ZnS have been proved to be excellent materials for tailoring the functions of 2DM aerogels, including the magnetism, electron conductivity, and photocatalysis. For instance, Bei *et al.* reported a highly dense graphene aerogel (HDGA) loaded with gold nanoparticles (AuNPs) for sensitive electrochemical detection of hydroquinone and catechol.[90] AuNPs have excellent electron conduction and electrocatalytic properties, which can specifically catalyze the redox reaction of hydroquinone, and the obvious synergistic effect between HDGA and AuNPs can better improve the ability of electron transport and mass transfer.

As shown in Fig. 3a, Lin *et al.* synthesized a kind of Z-type Ag–AgBr/$BiVO_4$/graphene aerogel (Ag–AgBr/$BiVO_4$/GA) photocatalyst by simply hydrothermal loading Ag–AgBr NPs and $BiVO_4$ nanocrystals onto GA.[91] The original Ag–AgBr NPs have high photocatalytic performance for the degradation of organic matter or bacteria. The heterojunction formed by combining with $BiVO_4$ and GA can effectively promote the absorption of visible light and the separation of photogenerated carriers. Meanwhile, the surface plasmon resonance (SPR) of metal $Ag^{\circ}$ can also promote the absorption of visible light and the transport of charge. Therefore, the created Ag–AgBr/$BiVO_4$/GA exhibited significant photocatalytic activity against methyl

 

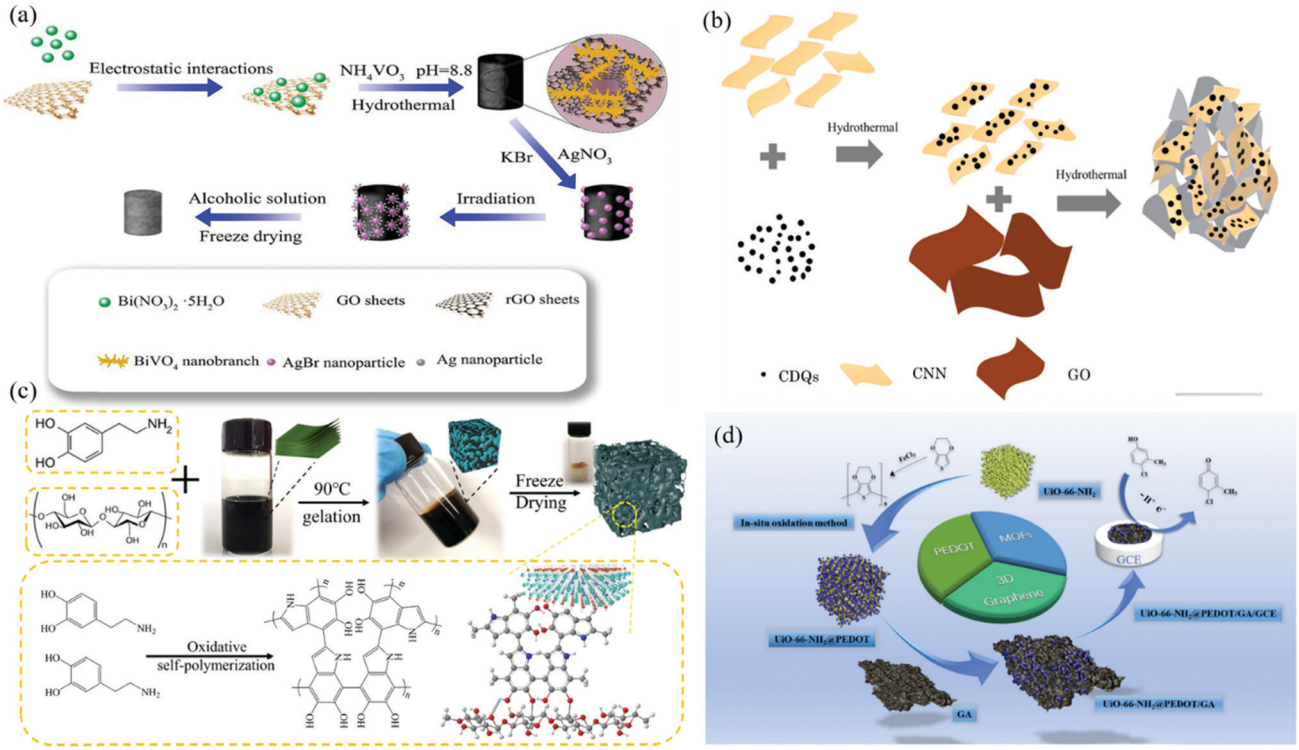


Fig. 3 Functional tailoring of 2DM aerogels: (a) Preparation schematic diagram of Ag–AgBr/$BiVO_4$/GA composite.[91] Copyright 2020, Elsevier. (b) Preparation diagram of GA-CQDs/CNN.[95] Copyright 2018, Elsevier. (c) Synthetic route diagram of P-M/MX-m composite aerogel.[102] Copyright 2021, Springer. (d) Preparation diagram of 3D UIO-66-$NH_2$@PEDOT/GA.[104] Copyright 2019, Elsevier.

orange (MO), *Escherichia coli* and *Staphylococcus aureus*. In another study, Chen and colleagues prepared 3D RGO-loaded $SnO_2$ NP composite aerogels by a simple hydrothermal method and then freeze-drying.[92] $SnO_2$ NPs are typical n-type metal oxide semiconductors, and the as-prepared 3D $SnO_2$/RGO composite aerogels present excellent sensing properties for $NO_2$ gas detection, such as high sensitivity, good linearity, and fast response. Li *et al.* synthesized multifunctional magnetic graphene oxide aerogels (M-RGOs) by *in situ* deposition of magnetic $Fe_3O_4$ NPs onto 3D GA by an one-pot solvothermal method.[93] Under the addition of magnetic $Fe_3O_4$ NPs, M-RGOs has been proved to be an ideal broad-spectrum adsorbent, showing excellent adsorption capacity for oils, organic solvents, arsenic ions, dyes, and other pollutants. In a similar study, Reddy *et al.* reported that a GA doped with zinc sulfide (ZnS) with magnetic and photocatalytic activity has good photocatalytic degradation ability for methylene blue (MB) and Cr(VI), and the magnetism of the composite makes it easy for recovery and subsequent separation.[94]

### 4.2. Addition of functional carbon nanomaterials

Carbon nanomaterials are a new type of functional materials that have attracted much attention, such as CNTs, carbon quantum dots (CQDs), graphene quantum dots (GQDs), and carbon nanospheres. Adding functional carbon nanomaterials to 2DM aerogels is known as a promising strategy to improve the properties of aerogels. As shown in Fig. 3b, He *et al.* loaded 0D CQDs onto 2D g-$C_3N_4$ by hydrothermal method, and combined with 2D graphene to form 3D graphene–CQDs/g-$C_3N_4$ nanosheets (GA-CQDs/CNN) aerogels as visible photocatalysts.[95] When CQDs was loaded onto g-$C_3N_4$, type II van der Waals heterojunction was formed between them due to π–π stacking, which inhibited the charge recombination, and effectively promoted the separation of photogenerated electrons–holes. The resultant GA-CQDs/CNN showed a good visible light catalytic efficiency for MO (91.1%). Wan *et al.* reported a method to synthesize graphene–CNT aerogel (GCAs) by adding CNTs into GA.[25] CNTs with good toughness and hydrophobicity were mixed with GA to effectively improve the morphology, specific surface area, mechanical strength, and hydrophobicity of GA. The adsorption capacity of the improved GCAs for organic solvents reached 100–270 times of its own weight, holding the ability to withstand the weakening of the recovery and reuse steps (adsorption–combustion and adsorption–extrusion experiments). Kang *et al.* added positively charged magnetic carbon nanospheres (MCNS) to negatively charged GO by hydrothermal reduction and electrostatic self-assembly to synthesize magnetic carbon nanospheres/graphene composite aerogels (MCNS/NGA) as adsorbents.[96] The addition of MCNS enables MCNS/NGA to achieve directional adsorption through magnetic control technology, allowing rapid separation of pollutants under the action of external magnetic field.

### 4.3. Addition of polymers and biomaterials

The addition of natural synthetic polymers to 2DM aerogels has been proved to be a good strategy to improve the mechanical

properties and obtain additional functions of the aerogels.[97] Wang and colleagues constructed a new 3D oriented polypyrrole (PPy)/PVA/$C_3N_4$ nanosheet (NSs) heterojunction aerogel (marked as CNPVPy) by directional freezing.[18] 2D $C_3N_4$ nanosheets were assembled with conductive polymers to form p–n junctions, thus enhancing the charge separation and obtaining extensive absorption in the visible near infrared range. This oriented heterojunction aerogel without metal semiconductors has been proved to have excellent photocatalytic performance under visible light. Cao *et al.* reported a mild method for the synthesis of 3D aerogels (PSRGO aerogels) of PVA and SA crosslinked RGO sheets.[98] PVA not only improved the mechanical properties of aerogels, but also obtained amphiphilic properties, which endow the resultant aerogels with excellent adsorption capacity for organic solvents. In another study, Krittayavathananon and Sawangphruk modified single-strand DNA (ss-DNA) on reduced graphene aerogel ($RGO_{ae}$).[99] The impedance biosensor with ss-DNA/$RGO_{ae}$ as electrode can be used for quantitative determination of aflatoxin B1 (AFB1) in high temperature milk. ss-DNA was modified onto the surface of aerogel, and the phosphate group on ss-DNA provided negative charge, which increased the negative charge coverage at the electrode interface and can also recognize aflatoxin by a lock and key process.

Wu *et al.* reported the synthesis of functional chitosan/graphene oxide (CS/GO) composite aerogel microspheres by supercritical $CO_2$ drying.[100] CS chains and GO were connected by electrostatic interaction and hydrogen bonding. Many amino and hydroxyl groups in CS enable CS to effectively adsorb anionic organic dyes and heavy metal ions through electrostatic interaction or chelation. In another case, Ribeiro and colleagues synthesized porous, ultra-light, and self-supporting bacterial nanocellulose (BC)/$MoS_2$ hybrid aerogels by hydrothermal method.[101] The carrier BC aerogel for controllable growth of $MoS_2$ has unique structure and properties, including highly porous 3D structure, flexibility, low density, and mechanical stability. The specially designed BC/$MoS_2$ aerogel film showed good photocatalytic degradation of MB and heavy metal ions under visible light irradiation, and also had good recyclability. Zhang *et al.* reported a PDA-functionalized cellulose/MXene composite aerogel (denoted as P-M/MX-m composite aerogel) prepared by oxidative self-polymerization and freeze-drying,[102] as shown in Fig. 3c. Cellulose aerogel can provide 3D framework and porous structure. PDA has many functional groups and can combine with organic dyes in wastewater. The obtained P-M/MX-m composite aerogel exhibited excellent adsorption capacity for MB in salt water.

### 4.4. Addition of other substances

Some other functional materials, such as silica, indium vanadate, metal–organic frameworks (MOFs), Prussian blue analogues, layered double hydroxides, and ionic liquids, can also be added to 2DM aerogels to tailor their functions. Zheng *et al.* prepared GO/silica-based composite aerogels by a simple *in situ* sol–gel reaction.[103] The co-hydrolysis and condensation between trimethoxymethylsilane (MTMS), dimethoxydimethylsilane (DMDMS) and GO treated with 3-glycidoxypropyl trimethoxysilane (GPTMS) formed the Si–O–Si bond, constituting a double cross-linking

Table 1 Functional tailoring of 2DM-based aerogels

| 2DM aerogels | Synthesis method | Regulation method | Characteristic | Ref. |
|---|---|---|---|---|
| Graphene–gold nanostar | Self-assembly, freeze-drying | Adding gold nanostar | Enhanced electrocatalytic activity | 90 |
| Ag–AgBr/$BiVO_4$/graphene | Hydrothermal, freeze-drying | Adding $BiVO_4$ and Ag–AgBr NPs | Enhanced absorption of visible light and separation of photo-generated carriers | 91 |
| $SnO_2$/RGO | Hydrothermal, freeze-drying | Adding $SnO_2$ nanocrystals | Large surface area, high electrical conductivity | 92 |
| $Fe_3O_4$–RGO | Solvothermal, freeze-drying | Adding $Fe_3O_4$ NPs | Magnetic | 93 |
| ZnS–graphene | Self-assembly, freeze-drying | Adding ZnS | Enhanced photocatalytic activity and stability | 94 |
| Graphene–CQD/g-$C_3N_4$ nanosheet | Hydrothermal, freeze-drying | Adding CQDs | Excellent charge separation efficiency and visible light absorption capacity | 95 |
| Graphene–CNT | Hydrothermal, freeze-drying | Adding CNTs | Enhanced hydrophobicity and mechanical strength | 25 |
| Carbon nanospheres/graphene | Hydrothermal self-assembly, freeze-drying | Adding carbon nanospheres | High specific surface area and magnetic properties | 96 |
| $C_3N_4$–PPy | Self-assembly, freeze-drying | Directional freezing, adding PPy and PVA | Aligned porosity, high stability, effective charge separation | 18 |
| PVA/SA/RGO | Hydrothermal self-assembly, freeze-drying | Adding PVA and stearic acid | Excellent mechanical properties and oleophilic | 98 |
| ss-HSDNA/RGO | Hydrothermal, freeze-drying | Adding ss-HSDNA | Enhanced electrocatalytic activity | 99 |
| CS/GO aerogel microspheres | Self-assembly, $CO_2$ supercritical drying | Adding chitosan | Large surface area and good biocompatibility | 100 |
| BC/$MoS_2$ | Hydrothermal, $CO_2$ supercritical drying | Adding bacterial nanocellulose | High surface area and pore volume and stability | 101 |
| Cellulose-MXene | Oxidative self-polymerization, freeze-drying | Adding cellulose | Light weight, high structural stability and high porosity | 102 |
| GO/silica | Sol–gel reaction, atmospheric drying | Adding silica | Excellent mechanical properties and thermal stability | 103 |
| UiO-66-$NH_2$@PEDOT/graphene | Hydrothermal, freeze-drying | Adding MOF UiO-66-$NH_2$ and PEDOT | High conductivity, large specific surface area and fast electron transfer rate | 104 |
| MXene-Prussian blue aerogel spheres | Atmospheric drying | Adding Prussian blue | Large specific surface area, hydrophilicity, and ion-exchange behavior | 105 |

 

network. The existence of silica provides flexibility for the aerogel as a whole. As shown in the Fig. 3d, Tian *et al.* synthesized UiO-66-$NH_2$@PEDOT with core–shell structure on the surface of Zr-based metal organic skeleton (UiO-66-$NH_2$) by *in situ* polymerization of (3,4-ethylenedioxythiophene) (PEDOT).[104] The modified electrode composed of GA as the substrate material of UiO-66-$NH_2$@PEDOT was used as an electrochemical sensor for the detection of 4-chloro-3-methylphenol (PCMC). In this case, PEDOT was used to enhance electrochemical sensing performance due to its excellent electrocatalytic activity and high conductivity. UiO-66-$NH_2$ formed an open porous 3D structure, which could load PEDOT. Therefore, the formed UiO-66-$NH_2$@PEDOT showed a good linear range of 0.6–18 μM for the detection of PCMC with a low detection limit of 0.2 μM. Lee and co-workers reported a titanium carbide MXene ($Ti_3C_2T_x$)/Prussian blue aerogel microsphere (PB-$MX_{sphere}$) as an adsorbent for radioactive cesium.[105] Among them, Prussian blue is a six-annotation ferrate, which is a safe and non-toxic material that can be used to selectively capture radioactive cesium in cages. The as-synthesized PB-$MX_{sphere}$ can maintain high adsorption capacity of cesium in high salt and extreme pH environments.

### 4.5. Summary

In order to make it more clear for the above introduction, here we summarize the functional tailoring of 2DM aerogels in Table 1.

## 5. Monitoring hazards in environment with 2DM aerogels

2DM aerogels have been proved to hold broad prospects in the field of pollutant detection. Compared with pure 2DMs, 2DM aerogels not only maintain excellent optical and electrical properties, but also possess high specific surface area and more ''vacancies'' for fixing identifiers.[106] At present, 2DM aerogels have been applied as materials for the fabrication of optical and electrochemical sensors for the detection of pollutants. Optical sensors have been widely used in pollutant detection because of their high sensitivity and green environmental protection. The principles of the optical sensors are to use the recognition element to interact with the sample by producing chemical or physical changes, such as Raman scattering, fluorescence, resonance light scattering, refractive index or absorbance change.[107] Compared with optical sensors, electrical sensors are more widely used in the field of pollutant detection because of their fast response, favorable sensitivity, and selectivity as well as simple operation. The principles are based on the change of the object to be measured produces an electrical signal.[108] In this part, we focus on the use of 2DM aerogels as sensors for the detection of inorganic pollutants, organic pollutants, gas pollutants and solid surface pollutants in water.

### 5.1. Monitoring inorganic pollutants in water

Inorganic pollutants in water, such as heavy metal ions and some anions, can be detected by sensors based on 2DM aerogels. As shown in Fig. 4a, Zhi *et al.* prepared graphene-doped $MoS_2$ aerogels (Au/$Fe_3O_4$/$MoS_2$ CAs) loaded with Au and $Fe_3O_4$ NPs by hydrothermal synthesis and assembly.[109] The resulting composite aerogels showed interconnected macroporous networks (Fig. 4b), and $Hg^{2+}$ in aqueous solution was detected sensitively at a low detection limit (3.279 nM) by colorimetric sensing (Fig. 4c). The colorimetric detection principle of composite aerogel towards $Hg^{2+}$ is that citric acid-capped AuNPs has catalase mimic activity, while 3,3′,5,5′-tetramethylbenzidine (TMB) can be oxidized by $H_2O_2$ and appear blue in the presence of catalase (Fig. 4d).[110]

Lu *et al.* used solvothermal method to combine GA and MOF (UiO-66-$NH_2$) to prepare GA-UiO-66-$NH_2$ complex for electrochemical detection of heavy metal ions in aqueous solution.[111] GA provides a matrix for *in situ* growth of UiO-66-$NH_2$ crystals and excellent electrical conductivity, while UiO-66-$NH_2$ provides active sites for binding to heavy metal ions. There is a good synergistic effect between GA and UIO-66-$NH_2$ crystals, which makes the composite electrode have a good response to heavy metal ions. Using the composite as a modified electrode, $Cd^{2+}$, $Pb^{2+}$, $Cu^{2+}$, and $Hg^{2+}$ in water were detected sensitively and simultaneously. In another case, Ma *et al.* reported a tungsten disulfide ($WS_2$)/RGO aerogel (rGA) composite $WS_2$/rGA synthesized by a solvothermal method.[112] $WS_2$ nanosheets were anchored onto the 3D porous network of rGA. The abundant active sites provided by $WS_2$ nanosheets and the high electron transfer rate provided by RGO network accelerated the electrochemical oxidation of nitrite, thus improving the electrocatalytic activity of the composite electrode for nitrite oxidation. The as-synthesized $WS_2$/rGA composite exhibited high selectivity and reproducibility, which could be used as electrochemical platforms for sensitive detection of nitrite in aqueous solution.

### 5.2. Monitoring organic pollutants in water

2DM aerogels are often used to detect organic pollutants in water, such as phenols, dyes, and pesticides that are harmful to the environment and human body. Xie *et al.* synthesized PPy@ZIF-8/GAs with layered porous structure by the hydrothermal method and *in situ* growth method using PPy as cross-linking agent.[113] Because ZIF-8 molecular sieve grown *in situ* has abundant active sites, 3D GAs presented excellent electrical conductivity and high specific surface area, and there was a good synergistic effect among PPy, Gas, and ZIF-8. The fabricated sensor with PPy@ZIF-8/GAs as electrode showed high sensitivity to highly toxic 2-methylene bis (4-chlorophenol) (dichlorophenol, Dcp), and the lowest detection limit was 0.1 nM. Moreover, the sensor has good reproducibility, selectivity, and stability for the detection of Dcp, which was suitable for the determination of Dcp in lake water samples. Yang and colleagues prepared Ag/g-$C_3N_4$/RGO aerogel (Ag/g-$C_3N_4$/RGOA) with surface enhanced Raman scattering (SERS) activity by one-pot hydrothermal method.[22] Thanks to its good SERS activity, the composite aerogel could detect rhodamine 6G (R6G) at a low detection limit ($1 \times 10^{-7}$ M).

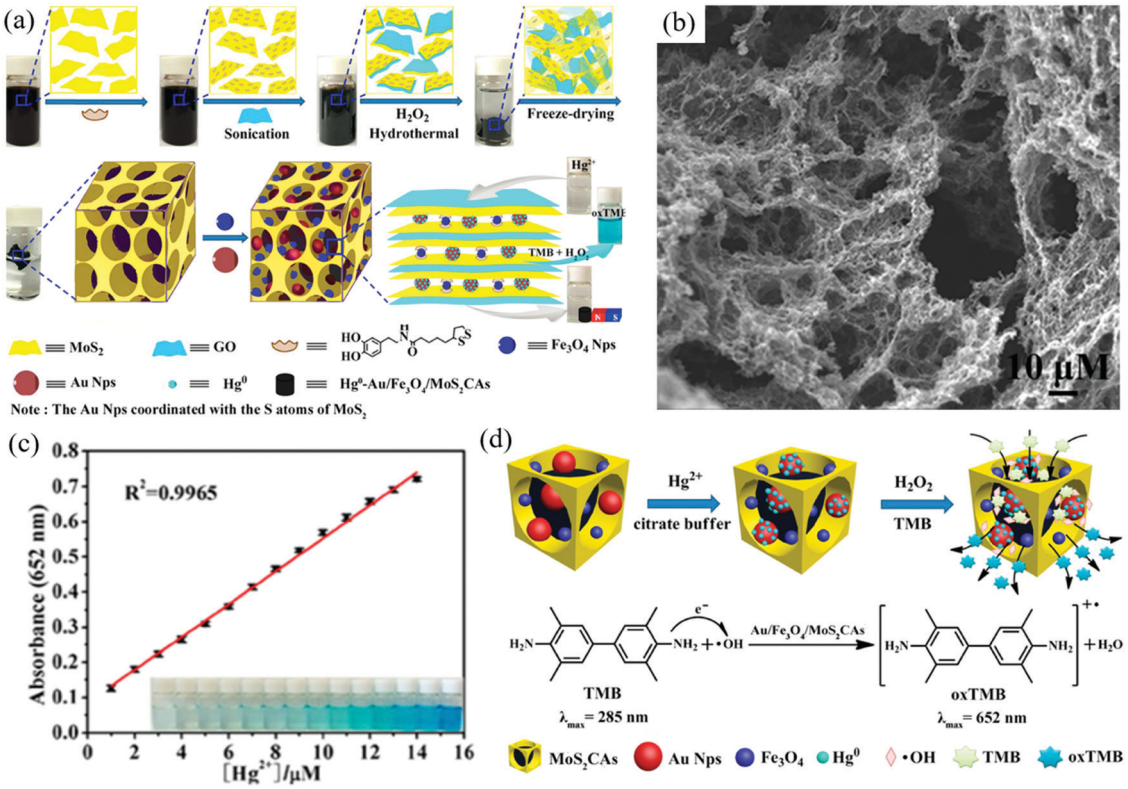


Fig. 4 Colorimetric detection of $Hg^{2+}$ with 2DM aerogels: (a) The growth mechanism of Au/$Fe_3O_4$/$MoS_2$ CA. (b) The SEM diagram of Au/$Fe_3O_4$/$MoS_2$ CA. (c) The relationship between the absorption response of the detection system and the concentration of $Hg^{2+}$. (d) The detection mechanism of $Hg^{2+}$ detection by Au/$Fe_3O_4$/$MoS_2$ CAs.[109] Copyright 2016, American Chemical Society.

Kokulnathan and Chen embedded gadolinium oxide nanorods into GA for highly selective electrochemical detection of pesticide carbendazim (CDM).[114] Mahpishanian and Sereshti prepared a magnetic 3D graphene aerogel composite (3D-G-$Fe_3O_4$).[115] Because of the highly interconnected network structure and magnetism of aerogel materials, the material has excellent extraction ability for organophosphorus pesticides (OPP). The aerogel composite can be used for magnetic solid phase extraction (MSPE) of OPP in fruit juice samples before gas chromatography–nitrogen phosphorous detection (GC-NPD). The method is very simple, environmentally friendly, and sensitive, and can be used as a routine tool for monitoring various pesticides in fruit juice. In another case, Sawangphruk *et al.* coated layered $MnO_2$ nanosheets onto nitrogen-doped RGO aerogel (3D-N-rGO) rotating disk electrode (RDE) by scalable electrodeposition.[116] The layered structure of $MnO_2$ can provide fast ion transport, so the sensor using $MnO_2$/3D-N-rGO RDE as electrode for the detection of hydrazine has low detection limit (0.085 μM), low response time (<2 s), wide linear range, and very good selectivity (proved by not disturbed with high concentrations of glucose, caffeine, methylamine, ethylenediamine, *n*-butylamine, adenine, cytosine, guanine, and L-arginine). In addition, the fabricated $MnO_2$/3D-N-rGO RDE sensor was expected to be used for the determination of trace hydrazine in drinking water and lake water and other real samples.

### 5.3. Monitoring air pollutants

Currently, the detection of air pollutants using 2DM aerogels as sensors is mainly focused on the monitoring of nitrogen oxides, sulfur oxides, and volatile organic compounds (VOCs). Long *et al.* synthesized $MoS_2$/graphene composite aerogel by supercritical drying and freeze-drying.[117] The fabricated aerogel showed ultra-low detection limit for $NO_2$ at room temperature. When the material was integrated into a microheater and heated to 200 °C, a final signal response of 90% and a recovery time of less than one minute can be achieved. Due to the organic combination of graphene and $MoS_2$, the material presented high specific surface area, electrical conductivity, and thermal conductivity of graphene and the high sensitivity and selectivity of $MoS_2$ to $NO_2$. In another study, they also prepared one-component $MoS_2$ aerogels with high performance by freeze-drying and two-step vulcanization for the detection of $NO_2$.[118] The $MoS_2$ aerogel maintained the previously reported low detection limit and fast response and recovery on a 200 °C microheater. Specifically, they confirmed that the p-type sensing behavior of $MoS_2$ aerogel was controlled by its defect state. Meanwhile, they changed the defect state of $MoS_2$ aerogel by thermal annealing, and the $MoS_2$ aerogel changed from p-type sensing behavior to n-type sensing behavior clearly.

Inspired by the studies of Long and co-workers, Ikram *et al.* synthesized vertically grown $MoS_2/C_3N_4$ mixed aerogels using a two-step method as a sensor assembly for the detection of

 

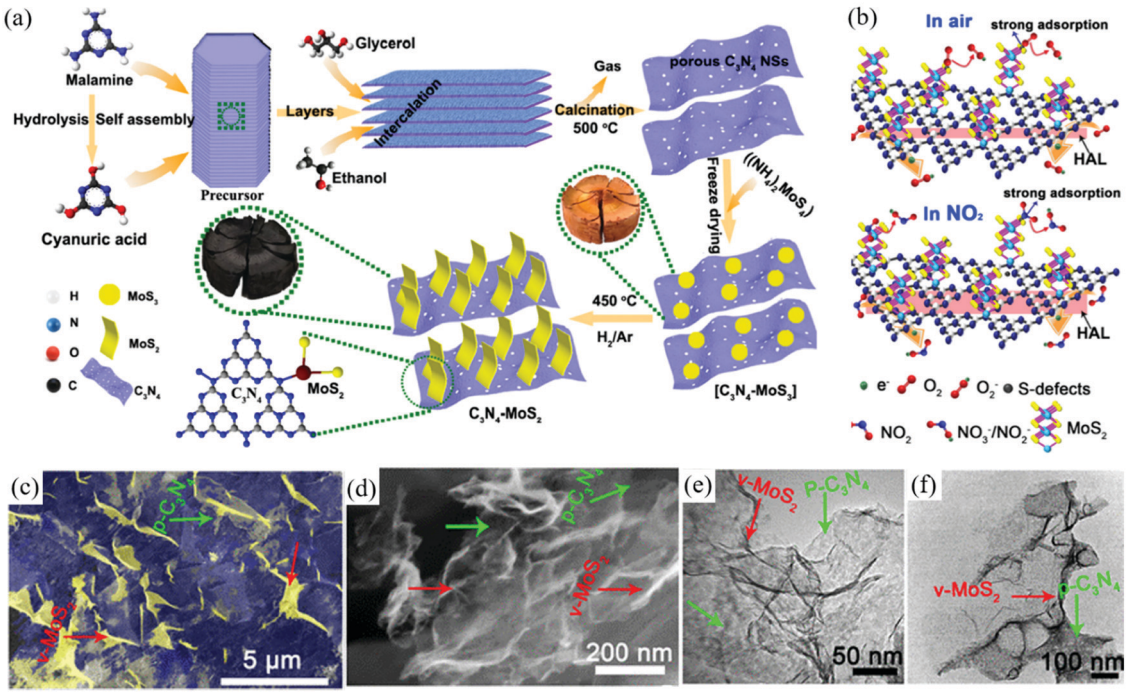


Fig. 5 Monitoring of air pollutants with 2DM aerogels: (a) Schematic diagram of two-step preparation routes of $C_3N_4$ NSs and $MoS_2$@$C_3N_4$ aerogels. (b) Schematic diagram of the sensor exposed to $NO_2$ gas in air and at room temperature. (c and d) SEM images of $MoS_2$@$C_3N_4$ aerogels. (e and f) TEM images of $MoS_2$@$C_3N_4$ aerogels.[106] Copyright 2020, American Chemical Society.

$NO_2$ (Fig. 5a).[106] The sensor showed long-term stability, low detection limit (10 ppb), high response speed ($R_a/R_g$ = 61.07–50 ppm), and very short response/recovery time (2.1 s and 35.7 s), as shown in Fig. 5b. This is mainly due to the 3D porous structure (Fig. 5c–f), high surface area, n–p junction, and excellent electrical conductivity of the aerogel. Maboudian and co-workers reported that a porous independent $WS_2$ aerogel could be used as a gas sensor.[119] The gas sensor was made by integrating $WS_2$ aerogel into the micro-heater platform. The sensor had a strong sensing ability to $NO_2$ in the absence of oxygen, and the response of the sensor to reducing gas ($H_2$ and $NH_3$) was obviously enhanced in the aerobic environment.

Metal oxides such as ZnO, $Fe_3O_4$, $SnO_2$, $Co_3O_4$, and CuO combined with 2DM aerogels can be used to detect VOCs. For instance, Guo *et al.* reported a RGO/$SnO_2$ p–n heterojunction aerogel prepared by a simple sol–gel method.[120] In RGO/$SnO_2$ p–n heterojunction aerogel, n-type $SnO_2$ NPs were connected to p-type RGO layer to construct the p–n heterojunction structure. The sensor using the aerogel as the sensitive layer coating of the microelectrode array had a good sensitivity for the detection of phenol at room temperature (the lowest detection limit was as low as 5 ppb), and the output signal has an obvious linear relationship with the concentration of phenol in the range of 10–80 ppb. In another case, Wang *et al.* used a hydrothermal method to attach CuO NPs into a highly interconnected porous network of MXene ($Ti_3C_2T_x$) and RGO to fabricate MXene/RGO/CuO aerogels.[23] The fabricated sensor based on MXene/RGO/CuO aerogel exhibited a response rate of 52.09% to 100 ppm acetone at room temperature, fast response and recovery speed (6.5 s and 7.5 s), as well as good selectivity and stability. Maboudian *et al.* loaded PtNPs onto BN aerogels with high specific surface area and high thermal stability.[121] Pt-loaded BN aerogel has high thermal conductivity and low density, which could be used for the calorimetric detection of propane when integrated on a micro-heater platform. It has the characteristics of low power consumption (<1.5 mW) and fast response and recovery time (<2 s).

### 5.4. Monitoring pollutants on solid surfaces

2DM aerogels are proved to be useful to detect the surface and internal contaminants of solids (especially food). Sun and colleagues immobilized glutamate-modified GQDs (Glu-GQD) and gold nanostars (Glu-GQD/Au) onto GA for the formation of composite materials, which could be used for the detection of acetamiprid, an insecticide on vegetables.[122] Glu-GQD/Au was covalently linked with acetamiprid aptamer (APT) to form a redox probe. The aptamer can specifically bind to acetamiprid and produce sensitive electrochemical reactions. Therefore, the differential pulse voltammetry signal generated by the electrochemical sensor can linearly decrease with the increase of acetamiprid concentration in the range from 1.0 fM to 1.0 × $10^5$ fM. The detection limit was 0.37 fM (S/N = 3), which can be adopted to the electrochemical determination of acetamiprid in vegetable environment.

Ma *et al.* modified β-cyclodextrin (β-CD) onto GAs for electrochemical detection of carmine 4R in food.[123] The as-prepared β-CD/GAs composites can recognize carmine 4R by host–guest interaction. In addition, there was an excellent

Table 2 Application of 2DM-based aerogel sensor in pollutant monitoring

| 2DM-based aerogel sensors | Analytes | Samples | Linear range | LOD | Ref. |
|---|---|---|---|---|---|
| $Au/Fe_3O_4/MoS_2$/graphene | $Hg^{2+}$ | Aqueous solutions | 1–14 μM | 3.279 nM | 109 |
| UiO-66-$NH_2$/graphene | $Cd^{2+}$, $Pb^{2+}$, $Cu^{2+}$ and $Hg^{2+}$ | Soil and vegetable | 0.06–3 μM ($Cd^{2+}$), 0.01–4 μM ($Pb^{2+}$), 0.1–3.5 μM ($Cu^{2+}$), 0.005–3 μM ($Hg^{2+}$) | 9 nM ($Cd^{2+}$) 1 nM ($Pb^{2+}$) 8 nM ($Cu^{2+}$) 0.9 nM ($Hg^{2+}$) | 111 |
| $WS_2$/RGO | Nitrite | Spiked bacon | 0.01–130 μM | 3 nM | 112 |
| Polypyrrole@ZIF-8/graphene | 2,2-Methylenebis (4-chlorophenol) | Lake water | $3 \times 10^{-10}$–$1 \times 10^{-5}$ M | 0.1 nM | 113 |
| Ag/g-$C_3N_4$/RGO | R6G | Wastewater | — | $1 \times 10^{-7}$ M | 22 |
| GdO/graphene | Carbendazim | Aqueous solutions | 0.01–75 μM | 3.0 nM | 114 |
| $Fe_3O_4$–graphene | Pesticide carbendazim | Juice samples | 3–50 000 ng $L^{-1}$ | 1.2–3.1 ng $L^{-1}$ | 115 |
| $MnO_2$/RGO | Hydrazine | Drinking water and lake water | — | 085.0 μM | 116 |
| $MoS_2$/graphene | $NO_2$ | — | — | 50 ppb | 117 |
| $MoS_2$ | $NO_2$ | — | — | 50 ppb | 118 |
| $MoS_2/C_3N_4$ | $NO_2$ | — | — | 10 ppb | 106 |
| $WS_2$ | $NO_2$, $H_2$ and $NH_3$ | — | 0.2–3 ppm ($NO_2$) 50–5000 ppm ($H_2$) 50–800 ppm ($NH_3$) | 8 ppb ($NO_2$) 60 ppm ($H_2$) 13 ppm ($NH_3$) | 119 |
| $SnO_2$/RGO | Phenol | — | 10–80 ppb | 5 ppb | 120 |
| MXene/RGO/CuO | Acetone | — | 10–500 ppm | — | 23 |
| Pt/BN | Propane | — | 5000–20 000 ppm | — | 121 |
| Glu-GQD/Au–Apt/graphene | Acetamiprid | Vegetables | 1.0–$1 \times 10^5$ fM | 0.37 fM | 122 |
| β-Cyclodextrin/graphene | Ponceau 4R | Food samples | 1.0 nM–1.0 μM | 0.3 nM | 123 |
| RGO | Quercetin | Ginkgo tablets | 0.1–100.0 μM | 0.065 μM | 124 |

synergistic effect between β-CD and GAs. The electrical signal produced by β-CD/GAs electrode maintained a good linear relationship in the range of 1.0 nM–1.0 μM with a detection limit of 0.3 nM, presenting good repeatability and anti-interference ability. Niu *et al.* synthesized 3D RGO aerogel (3D-RGA) with unique pore structure through a one-step hydrothermal method.[124] The 3D-RGA aerogel was used as a modified electrode of carbon ionic liquid electrode (CILE) for sensitive determination of quercetin in ginkgo tablets with a detection limit of 0.065 μM.

To summarize the above introduction and discussion, a table on the application of 2DM aerogels for pollutant monitoring is presented here (Table 2).

# 6. Remediation of environmental pollutants with 2DM aerogels

## 6.1. Adsorption and removal of pollutants

Compared with other environmental remediation methods (such as *in situ* combustion, biodegradation, biological separation, and membrane filtration, *etc.*), the adsorption has been considered to be one of the most effective, economical and green ways to treat industrial wastewater.[125] There are many kinds of adsorbents for sewage treatment, such as activated carbon, zeolite, clay, metal–organic framework, as well as cellulose- and polymer-based composites. However, these traditional materials are limited by low adsorption capacity, poor recyclability and other conditions in practical application. 2DM-based aerogels are one of the most ideal adsorbents because of their low density, high porosity, large specific surface area, high mechanical strength, and chemical stability. The 2DM-based aerogel after structure and functional tailoring can have excellent elasticity and flexibility, which is an ideal adsorbent for sustainable recycling. This part will introduce the application of 2DM aerogels in the adsorption of inorganic pollutants (such as metal cations and radionuclides) and organic pollutants (oils, organic solvents, dyes, and other organic compounds) in water.

**6.1.1. Adsorption of inorganic pollutants in water.** Heavy metal ions are harmful to human body and ecological environment because of their high toxicity, difficult to be biodegraded, and can be enriched through the food chain. 2DM aerogels are good adsorbents for heavy metal ions.

Liu *et al.* synthesized 3D graphene/δ-$MnO_2$ aerogels by hydrothermal self-assembly of GO and *in situ* growth of δ-$MnO_2$.[126] The saturated adsorption capacities of the aerogel for $Pb^{2+}$, $Cd^{2+}$, and $Cu^{2+}$ were 643.62, 250.31, and 228.46 mg $g^{-1}$, respectively, which were much higher than that of the single GA. This mainly depends on that the lamellar gap of δ-$MnO_2$ on the surface of graphene aerogel can provide a place for heavy metal ions to exchange with pre-embedded $K^+$ ions. As shown in Fig. 6a, Kabiri *et al.* combined porous silicon in two kinds of natural diatoms with graphene from graphite through self-assembly, and the biomimetic graphene–diatom aerogel has a 3D network similar to that of natural graphite and siliceous rock (Fig. 6b and c).[127] Under the influence of the oxygen functional groups of amino and graphene on the modified diatom surface and iron oxide NPs, the formed aerogel showed excellent affinity to $Hg^{2+}$, and could reach an adsorption capacity greater than 500 mg $g^{-1}$ (Fig. 6d). Different from the addition of metal oxides to aerogels, Fang *et al.* prepared 3D LDH/GO aerogels by cross-linking GO layers with LDH. The hydrophilicity of the aerogels greatly improved the adsorption of $Cd^{2+}$ in water.[128]

 

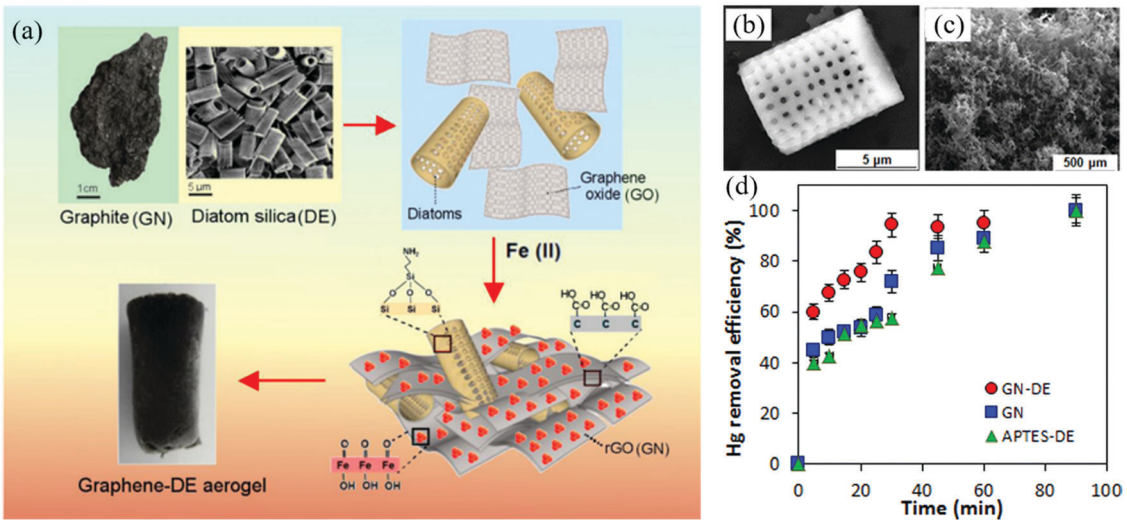


Fig. 6 Adsorption of $Hg^{2+}$ with GN-DE aerogel: (a) Synthetic schematic diagram of graphene-diatom silica aerogel. (b and c) SEM image of graphene-diatom silica aerogel. (d) Time dependence of $Hg^{2+}$ adsorption on GN-DE aerogel, graphene (GN) aerogel (with α-FeOOH nanoparticles), and APTES-modified diatom (APTES-DE).[127] Copyright 2015, American Chemical Society.

Nuclear waste sewage contains a number of radionuclides, which pose a great threat to human health and ecological environment. Cesium is a common radionuclide.[129] Hexacyanoferrate, also known as Prussian blue (PB) and Prussian blue analogues (PBAs), is a special adsorbent for cesium.[130] It has been proved that loading PB onto 2DM aerogels is a facile strategy for absorbing cesium. For instance, Lee *et al.* promoted the reductive self-assembly of GO and the cross-linking with PVP by γ-ray irradiation, and *in situ* formation of uniform PB NPs on the aerogel.[131] The PB@PVP/RGO aerogels were prepared after freeze-drying, which exhibited a double network structure and the cross-linking between rigid GO layers and flexible PVP chains. The formed aerogels not only has high mechanical strength and swelling ability, but also can quickly adsorb $Cs^+$ with high adsorption capacity (143.88 mg $g^{-1}$). Huo *et al.* prepared a Prussian blue analogue (3D RGO/PBAs) based on reduced graphene aerogel by chemical reduction and impregnation.[132] The adsorption capacity of the aerogel to $Cs^+$ reached 204.9 mg $g^{-1}$.

In another study, Fu *et al.* found that a new type of immobilized layered composite KMS-1/r-GO (KGO) can be prepared by hydrothermal growth of layered structure $K_{2x}Mn_xSn_{3-x}S_6$ (KMS-1) on RGO sheets.[133] The composite could remove radioactive ions $Cs^+$ and $Sr^{2+}$, by ion exchange and surface bonding interaction, and the maximum adsorption capacities of the two ions were 338.18 and 220.12 mg $g^{-1}$, respectively. In addition, the adsorbent showed good adsorption performance for radioactive ions in a wide range of pH, so the adsorbent had great significance in the removal of radioactive ions in wastewater. Li *et al.* prepared graphene oxide nanoribbons (GONRs) aerogels with 3D porous structure by hydrothermal method.[134] GONRs aerogel has large specific surface area and rich oxygen-containing groups, and can adsorb uranium(VI) and thorium(IV) with high efficiency. The maximum adsorption capacities of U (VI) and Th(IV) were 430.6 and 380.4 mg $g^{-1}$, respectively. In addition, the adsorbed ions were easy to be separated from water.

**6.1.2. Adsorption of organic pollutants in water.** Oil spill and organic pollutants have disastrous effects on the ecological environment, where 2DM aerogel is a good choice for the oil–water separation. There are no lipophilic groups on the surface of many 2DMs, and the modification of lipophilic groups on their surfaces to make them hydrophobic is the key for the application of oil–water separation. In addition, as a water–oil separation agent, the recyclability and reusability are particularly important, which requires high mechanical strength, compressibility, and flame retardancy of the designed 2DM aerogels, to facilitate the use of cyclic distillation, extrusion and combustion for recovery and reuse.

Song *et al.* reported a compressible 3D g-$C_3N_4$/PVA nanoflake aerogel.[135] Low density and high hydrophobicity endow the aerogel the ability to float on the water surface, which was more conducive to the solution of oil spills. In addition, the high mechanical strength and compressibility enable the aerogel to complete the renewable steps such as cyclic distillation, extrusion and combustion, and the adsorption capacity decreases little after the renewable cycle. Kang *et al.* synthesized novel magnetic carbon nanospheres/nitrogen-doped graphene composite aerogels (MCNS/NGA) through hydrothermal reaction and *in situ* electrostatic self-assembly of negatively charged GO sheets and positively charged magnetic carbon nanospheres (MCNS).[96] Under magnetic support, the oil gathering device with MCNS/NGA filter can achieve directional adsorption, with the adsorption capacity for oil and organic solvents reaching 187–537 g $g^{-1}$, and has also an excellent recoverability. Hou *et al.* added functional graphene nanoribbons (GONR) to the skeleton of GAs by a simple hydrothermal method to form reliable cross-linking.[136] After unidirectional freezing, the capillary layered porous structure was constructed for the aerogel, which enhanced the absorption of organic solvents by the aerogel,

which reached 98–447 times of its own weight. Wang *et al.* synthesized hydrophobic PI/MXene aerogel by combining polyimide (PI) with MXene ($Ti_3C_2T_x$).[12] The combination of the two components not only promoted the formation of porous framework through strong interaction, but also made MXene hydrophobic. The composite aerogel could quickly separate chloroform, soybean oil and liquid paraffin from water–oil system.

Wang and colleagues reported a physicochemical cross-linking method for the synthesis of porous BN aerogels.[13] The modified h-BN and carboxymethyl cellulose (CMC) formed hybrid aerogels by physical and chemical cross-linking and hydrogen bonding, and the pore structure of h-BN-based aerogels can be controlled by adjusting the concentration of cross-linking agent. The h-BN-based aerogel has a high specific surface area and its oil absorption capacity can reach 31.55 g $g^{-1}$, and the capacity does not decrease obviously after 6 cycles. Jiang *et al.* prepared an ultra-light BN nanoribbon (BNNR) aerogel by low-cost freeze-drying combined with high-temperature tube furnace heating using boric acid and melamine as B and N sources.[137] BNNR aerogel showed a porous structure and large specific surface area. It exhibited good adsorption properties for PEDOT:PSS (3-ethylenedioxythiophene: polystyrene sulfonate) (6020 mg $g^{-1}$) and mustard oil (5010 mg $g^{-1}$), and the applied aerogels could be cleaned and reused by combustion in air.

Heavy oil accounts for about 40% of the world's total oil. The high viscosity of heavy oil hinders the adsorption of aerogels. How to deal with high viscosity heavy oil is still a serious challenge. The common strategy to solve the problem of adsorbing heavy oil is to reduce the viscosity of heavy oil by heating. Inspired by wood structure, Fu and colleagues prepared superelastic, self-cleaning, and super-hydrophobic MXene aerogels by directional ice template method.[138] As shown in Fig. 7a, functionalized nanocellulose (f-NCC) and MXene are self-assembled in polyurethane to form hydrogels, which are freeze-dried and freeze-dried to form oriented porous MXene aerogels. As shown in Fig. 7b and c, MXene aerogel after directional freezing demonstrates a layered macroporous structure similar to wood structure, with axial channels connected to each other, which endow MXene aerogel with high adsorption capacity for a variety of oils (Fig. 7d) and good recyclability. Moreover, MXene aerogel also has extraordinary photothermal conversion ability (Fig. 7e). The temperature of MXene aerogel increased significantly after sunlight irradiation, the viscosity of heavy oil decreased significantly at high temperature, and the adsorption capacity of MXene to heavy oil was increased significantly. In another case, Hu *et al.* synthesized GA loaded with $CuFeSe_2$ by hydrothermal method and freeze-drying.[139] $CuFeSe_2$ with high photothermal conversion ability and GA with high adsorption capacity can effectively adsorb crude oil. After removing the light source, the crude oil can still be retained in the aerogel, which makes it more convenient for the collection of crude oil.

Dye wastewater from textile, pharmaceutical, and paper-making industries has a great impact on human health and ecological environment due to its high toxicity, complex structure, and difficult to degrade.[140] The PB/PVP/RGO aerogel reported by Lee *et al.* exhibited excellent adsorption capacity (44.73 mg $g^{-1}$) for MB. The dye molecules were rapidly adsorbed under the influence of capillaries and embedded in the double network structure under the action of hydrogen bonds. Zhang and colleagues synthesized PDA-functionalized cellulose/MXene composite aerogels (P-M/MX-m) by oxidative polymerization of dopamine and freeze-drying.[102] Due to the abundant functional groups of MXene and PDA, the synthesized P-M/MX-m showed excellent adsorption capacity for MB (168.93 mg $g^{-1}$). Notably, P-M/MX-m is more favorable for the adsorption of MB under high concentration of $Cl^-$ and

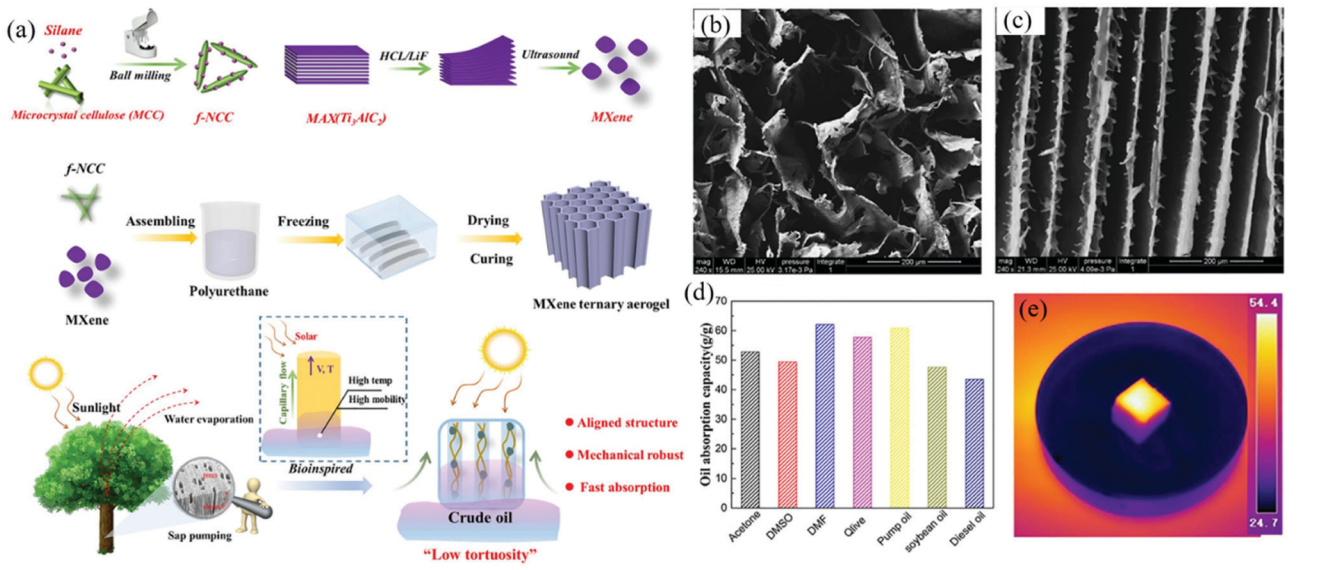


Fig. 7 Adsorption of organic dyes with MXene aerogels: (a) Schematic synthesis. (b) Cross-sectional morphology. (c) The longitudinal section morphology. (d) Oil absorption properties. (e) Infrared images of MXene aerogels floating on the water surface under solar radiation.[138] Copyright 2020, Elsevier.

 

thus can be used for the adsorption of dyes in high salt environment.

Guo *et al.* reported a $TiO_2$-decorated RGO aerogel ($TiO_2$-RGA) prepared by ethylenediamine reduction assisted hydrothermal method.[141] With the addition of appropriate amount of $TiO_2$, the whole aerogel was transformed from hydrophobic to hydrophilic, which increased the contact area between aerogel and polluted water containing RhB and improved the adsorption effect of RhB. Similarly, Wan *et al.* synthesized graphene–CNT aerogel (GCAs) by embedding CNTs into graphene network through ethylenediamine-assisted reduction hydrothermal method.[25] The addition of CNTs into GA improved the adsorption capacity and mechanical properties of GA. GCAs not only showed a good adsorption effect on MB and MO and other dyes, but also revealed good reuse ability.

**6.1.3. Capture of carbon dioxide.** Carbon dioxide ($CO_2$) is a greenhouse gas derived from the burning of fossil fuels, which causes environmental changes such as global warming, melting glaciers, sea level rise, *etc.*[142] At present, the method used to capture $CO_2$ is mainly absorbed by alkali solution, but it has some limitations including as high power consumption, equipment loss, and others.[143] In contrast, adsorption is regarded as one of the most suitable methods because of its high efficiency, low cost, safety, and environmental protection. Traditional adsorbents such as activated carbon,[144] zeolite,[145] and clay[146] have low adsorption capacity and poor recyclability, while 2DM aerogels offer better adsorption properties and good recycling capacity.

It has been proved that graphene aerogels combined with NB compounds,[147] chitosan,[148] hydrotalcite derived NPs,[149] and ionic liquids[150] can effectively capture $CO_2$. As shown in Fig. 8a and b, Xia *et al.* synthesized MgAl-mixed metal oxide/GO composite aerogel (MgAl-MMO/RGO composite aerogel) which can efficiently adsorb $CO_2$ through a simple three-step manufacturing process.[149] In the first step, LDH are attached to GO under the attraction of electrostatic interaction, and then LDH/GO hydrogels are formed with the help of molds and polymer additives. In the second step, LDH/GO hydrogel is transformed into LDH/GO aerogel with macroporous structure by unidirectional freezing and freeze-drying. In the last step, after thermal annealing in reducing atmosphere, LDH particles are transformed into MMO or metal nanoparticles (MNP), and finally MMO/RGO composite aerogels are formed. It can be seen from Fig. 8c–e that the aerogel has a macroporous structure grown by ice crystals and uniformly distributed MMO particles. Due to the 3D macroporous structure of aerogels and the increase of adsorption capacity of MMO particles, the MMO/RGO composite aerogels could reach the adsorption capacity of 2.36 mmol $CO_2$ per $g^{-1}$ (adsorbent) at the pressure of 8 bar and temperature of 300 °C (Fig. 8f).

Hsan *et al.* grafted cheap marine waste CS onto the surface of GO aerogel, and the ability of $CO_2$ adsorption of the aerogel

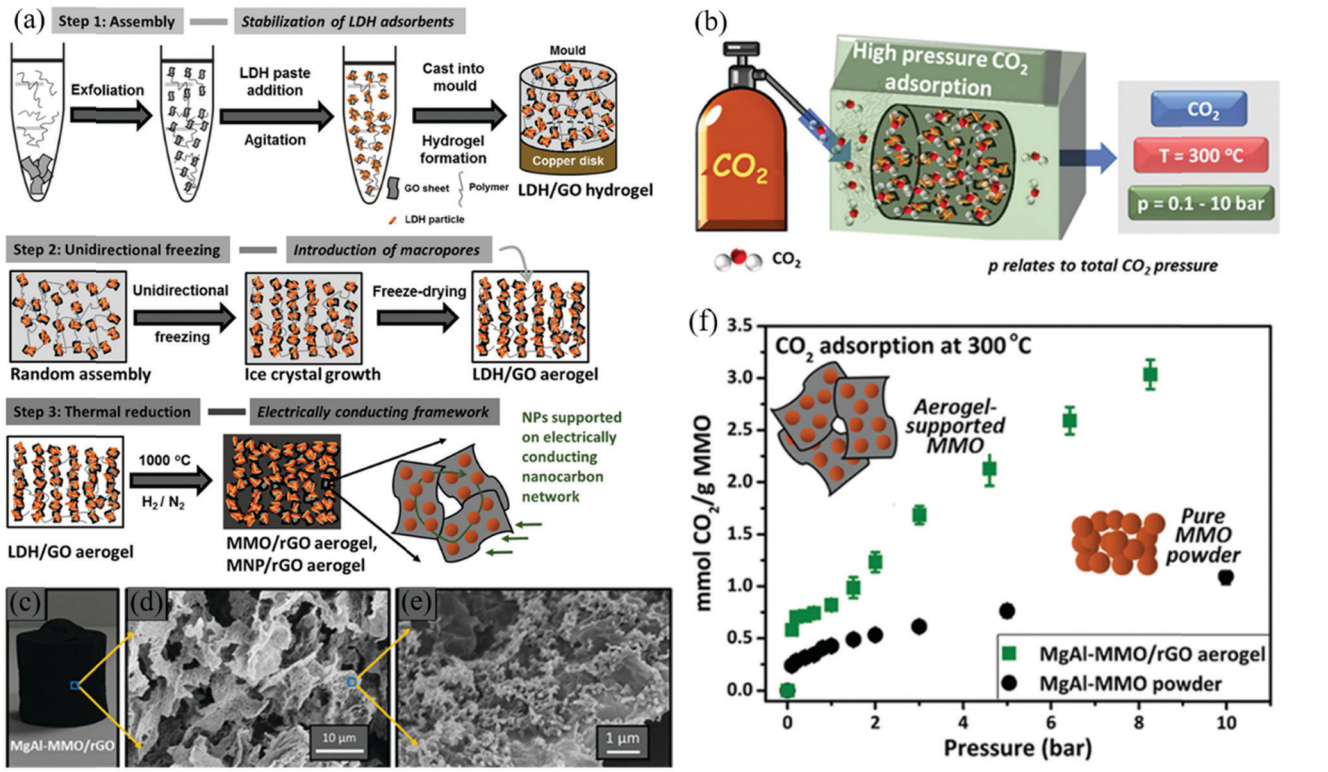


Fig. 8 Adsorption of $CO_2$ with MMO/RGO hybrid aerogel: (a) Synthesis process. (b) MgAl-MMO/RGO aerogel high pressure precombustion $CO_2$ adsorption schematic diagram. (c) Photograph of MgAl-MMO/RGO aerogel. (d and e) SEM images of MgAl-MMO/RGO aerogels. (f) The high-pressure $CO_2$ adsorption isotherm on MgAl-MMO powder and MgAlMMO/RGO aerogel under the condition of 300 °C and $CO_2$ total pressure of 0.210 bar.[149] Copyright 2020, Wiley-VCH.

was significantly higher than that of the pure CS.[148] Zeeshan *et al.* impregnated the ionic liquid 1-*N*-butyl-3-methylimidazole hexafluorophosphate ([BMIM][$PF_6$]) onto GAs to adsorb $CO_2$ with high selectivity.[150] Wang *et al.* used a 2D graphene plane as a template to synthesize a 3D silica aerogel on the graphene surface to form a sheet-like 2D/3D component.[151] The $CO_2$ adsorption capacity of the impregnated amine treated 2D/3D module reached the high value of 4.9 mmol $g^{-1}$ and remained stable in 10 cycles of $CO_2$ adsorption and desorption.

**6.1.4. Adsorption of VOCs.** Galiotis *et al.* assembled RGO and h-BN nanosheets together into 2D hybrid aerogels.[152] The preparation process of hybrid aerogel was simpler than that of pure h-BN aerogel, and its mechanical properties were better than that of pure GA. Compared with GA, the absorption capacity of formaldehyde and water vapor of composite aerogel were increased by about 7 and 8 times, respectively. Therefore, the formed hybrid aerogels could be used as VOC absorbents. Sun and colleagues assembled 2D $MnO_2$ nanosheets into ultralight $MnO_2$ aerogels by electroplating without the need for any functionalization or additional cross-linking agents.[153] The formation of $MnO_2$ aerogel was mainly due to the enhancement of van der Waals force between 2D layers, and these layers were arranged more orderly due to the influence of ice template method. The prepared $MnO_2$ aerogel revealed high porosity and strong oxidation ability, and could be used as an effective adsorbent for toxic reduction gas $N_2H_4$. Hsu *et al.* studied the adsorption performance of GA on polycyclic aromatic hydrocarbons in diesel vehicle exhaust by dynamometer.[154] Experiments show that GA has a significant adsorption effect on benzopyrene (310 ng $g^{-1}$), which is much higher than the commercially available XAD resin. In addition, GA can be recycled and reused. After three Soxhlet extractions and drying, the structure of GA remains basically unchanged.

**6.1.5. Capture of particulate matter.** Particulate matter (especially $PM_{2.5}$ with a diameter of less than 2.5 μm) is the main cause of haze problems,[155] which harms the health of human lungs and even damage the central nervous system.[156] At present, the main method used to capture $PM_{2.5}$ is to employ the 2D layered filter produced by electrospinning for adsorption.[157] The traditional 2D layered filter has some shortcomings, such as weak mechanical strength, small adsorption area, and poor recyclability. 2DM aerogel can make up for these shortcomings.

Zhao *et al.* prepared an electrified GA filter.[158] Under the action of electric field force, the removal efficiency of the filter reached 99% even at a very high concentration of PM ($>10\,000$ μg $m^{-3}$). Besides, it also has excellent stability, and the filter can still maintain a filtration efficiency of more than 99% after ten $PM_{2.5}$ cycles or five minutes of combustion. Zhang *et al.* prepared macroporous honeycomb aerogels by adding modified cyclic nanoparticles (mTNPs) to GA.[159] When the content of mTNP reaches 5wt%, the aerogel can capture $PM_{2.5}$ with a capture efficiency of 95.1%, and has a good ability for recovery and reuse. Lai and colleagues anchored zeolite imidazole framework-8 (ZIF-8) to GA with an *in situ* synthesis, and the resulting material showed excellent capture efficiency of $PM_{2.5}$ and $PM_{10}$ (99.3% and 99.6%), which could maintain high capture efficiency for a long time.[160]

As shown in Table 3, the adsorption performances of 2DM aerogels for various pollutants are summarized.

### 6.2. Photocatalytic degradation of pollutants

In addition to adsorption, photocatalytic redox reactions mediated by semiconductors have also attracted wide attention. The use of inexhaustible solar energy for the transformation of pollutants is a green, environmentally friendly, and safe. It is well known that the performance of photocatalyst depends largely on its chemical and physical structure, as they affect the three main steps of photocatalysis: photon absorption, carrier transfer, and catalytic surface reaction.[161]

2DM aerogels have the following advantages when used as photocatalytic pollutants. Firstly, 2DM aerogels have low density, high specific surface area, porosity, and electrical conductivity as well as 3D macroporous structure, endowing the aerogels with sufficient vacancy to embed semiconductor nanoparticles in the synthesis of photocatalysts, which can float on the polluted water surface. Meanwhile, the 2DM-based aerogels have excellent electrical conductivity, which effectively promote the efficiency of photogenerated electron transfer, thus improving the overall photocatalytic performance. Secondly, some 2DMs are semiconductors themselves, such as TMD/TMO, BP, and g-$C_3N_4$. 2D semiconductor materials with narrow band gaps that can consume photons in the visible region and induce electron–hole pairs ($e^-/h^+$) in the conduction and valence bands of semiconductors for redox reactions.[162–164] The aerogels of these 2DMs do not need to load other semiconductor nanoparticles and offer high photocatalytic activity that can oxidize and reduce pollutants in the solution. Finally, 2DM-based aerogels generally have good mechanical strength and compressibility, so that aerogels can be recycled by some methods to improve the sustainability and economy of the materials in order to facilitate further industrial production.[165] In this chapter, we will introduce 2DM aerogels for photocatalytic degradation of inorganic ions, dyes, and other organic pollutants as well as gases.

**6.2.1. Photocatalytic degradation of inorganic pollutants in water.** The 2DM aerogels can remove inorganic ions by photocatalysis, and it is common to reduce Cr(VI) to Cr(III). Due to its strong toxicity, carcinogenicity and fluidity in natural environment, hexavalent chromium [Cr(VI)] is a harmful pollutant which is widely produced in industrial processes such as leather making, pigment production and oil refining, and is difficult to deal with.

Chen *et al.* chose the flexible nonwovens blended with low melting point sheath-core polyester fiber and conventional polyester fiber (B-PET) as the carrier to support cellulose aerogel CA containing nano-flake g-$C_3N_4$, and prepared g-$C_3N_4$@CA/BPET with high flow impact strength.[27] Compared with g-$C_3N_4$ alone, g-$C_3N_4$@CA/B-PET revealed higher photocatalytic performance for hexavalent chromium and antibiotics, and also showed excellent reusability and light stability. Zhou's group prepared $MoS_2$/RGO aerogel photocatalyst by hydrothermal method and freeze-drying.[166] The addition of GO not

 

Table 3 Absorption capacity and reproducibility of 2D material-based aerogels for various pollutants

| 2DM aerogel adsorbents | Absorbing species | Adsorption capacity | Recyclability | Ref. |
|---|---|---|---|---|
| Graphene/δ-$MnO_2$ | $Pb^{2+}$, $Cd^{2+}$, $Cu^{2+}$ | 643.62 mg $g^{-1}$ ($Pb^{2+}$), 250.31 mg $g^{-1}$ ($Cd^{2+}$), 228.46 mg $g^{-1}$ ($Cu^{2+}$) | Maintain almost constant removal efficiency for $Pb^{2+}$ over eight desorption–regeneration cycles | 126 |
| Graphene–diatom silica | Mercury ions | >500 mg $g^{-1}$ | — | 127 |
| LDH/GO | Methylene blue, $Cd^{2+}$ | 96–125 mg $g^{-1}$ (MB) 95.67 mg $g^{-1}$ ($Cd^{2+}$) | — | 128 |
| Prussian blue/PVP/RGO | $Cs^+$, methylene blue | 143.88 mg $g^{-1}$ ($Cs^+$) 44.73 mg $g^{-1}$ (MB) | — | 131 |
| Prussian blue analogues/RGO | $Cs^+$ | 204.9 mg $g^{-1}$ | — | 132 |
| KMS-1/RGO | $Cs^+$, $Sr^{2+}$ | 338.18 mg $g^{-1}$ ($Cs^+$) 220.12 mg $g^{-1}$ ($Sr^{2+}$) | — | 133 |
| GONR | $U^{6+}$, $Th^{4+}$ | 430.6 mg $g^{-1}$ ($U^{6+}$) 380.4 mg $g^{-1}$($Th^{4+}$) | — | 134 |
| PVA/*g*-$C_3N_4$ | Pump oil, colza oil, olive oil, diesel oil, gasoline oil and organic solvents | 228–695 g $g^{-1}$ | The adsorption capacity can be maintained at 95% after 40 cycles | 135 |
| Carbon nanospheres/graphene | Dodecane, acetone, cyclohexane, pump oil, formamide, toluene, isopropanol, *n*-hexane, chloroform | 187–537 g $g^{-1}$ | 10 adsorption–combustion cycles give final adsorption capacity of 92.43% | 96 |
| GO/GONR-APTES | Carbon tetrachloride, dichloromethane, *n*-octane, pump oil, *etc* | 98–447 g $g^{-1}$ | Reuse after 10 cycles with retaining about 90% initial absorption capacity | 136 |
| Polyimide/MXene | Pump oil, chloroform, tetrahydrofuran, soybean oil, acetone, toluene, *n*-hexane, and waste pump oil | 18–58 g $g^{-1}$ | The aerogel collapsed after the fifth cycle | 12 |
| CMC/BN | Peanut oil, polydimethylsiloxane and lubricant oil | 31.55 g $g^{-1}$ | Over 6 cycles to absorb oil while maintaining a high capacity | 13 |
| BNNR | PEDOT:PSS and mustard oil | 6020 mg $g^{-1}$ (PEDOT: PSS) 5010 mg $g^{-1}$ (mustard oil) | After 4 cycles, the original adsorption rate of 37.6% is maintained | 137 |
| MXene | Pump oil, diesel oil, soybean oil, olive (light oil) and crude oil | 63 g $g^{-1}$ (light oil), 24.5 g $g^{-1}$ (crude oil) | Recyclability of 76% after 5 cycles (crude oil) | 138 |
| Graphene–$CuFeSe_2$ | Crude oil | 18.63 g $g^{-1}$ | After six cycles, the adsorption capacity is still greater than 18 g $g^{-1}$ | 139 |
| Cellulose/MXene | Methylene blue | 168.93 mg $g^{-1}$ | After five cycles, the removal efficiency could still maintain more than 84% for MB | 102 |
| $TiO_2$–RGO | Oleic acid and Rhodamine B | — | — | 141 |
| Graphene–CNT | Lube, *n*-hexane,ethanol, toluene, phenixin, methylene blue and methyl orange | 100–270 g $g^{-1}$ | After 10 cycles, the adsorption capacity hardly decreased | 25 |
| MgAl-mixed-metal-oxides/RGO | $CO_2$ | 2.36 mmol $g^{-1}$ | Recyclability of 95% after 5 cycles | 149 |
| CS/GO aerogel | $CO_2$ | 0.257 mmol $g^{-1}$ | — | 148 |
| Ionic liquid/RGO | $CO_2$ | — | — | 150 |
| Graphene–silica | $CO_2$ | 4.9 mmol $g^{-1}$ | Stable after 10 adsorption and desorption cycles | 151 |
| RGO/h-BN | Formaldehyde and water vapour | — | — | 152 |
| $MnO_2$ | $N_2H_4$ | — | — | 153 |
| Graphene | PMs | — | — | 158 |
| Large-sized GO | $PM_{2.5}$ | — | The aerogel can be used repeatedly and retain the high filtration efficiency after simple recycling | 159 |
| ZIF-8/Graphene | $PM_{2.5}$ and $PM_{10}$ | — | — | 160 |

only promoted the gelation in the hydrothermal reaction, but also accelerated the growth of 3D $MoS_2$ structure. The photoreduction rate of the obtained $MoS_2$/RGO aerogel to Cr(VI) was 92%, which was much higher than that of the single $MoS_2$ powder.

Duan *et al.* reported a $C_3N_5$/RGO aerogel with 3D macroscopic morphology.[167] Microscopic 2D/2D hybrid nanosheet with the Mott Schottky heterostructure was formed in the aerogel, which could not only expand the range of light response, but also effectively reduce the electron/hole recombination caused by photoexcitation, thus improving the photocatalytic efficiency. Under a low concentration of 10 ppm, the photoreduction removal rate of uranium(VI) wastewater containing organic matter reached 94.9%. Wang *et al.* synthesized graphene aerogel (GA-200) by hydrothermal method at 200 °C.[168] GA-200 converted uranium from soluble ions to insoluble ($UO_2$)$O_2{\cdot}2H_2O$ under visible light and air atmosphere, and the removal rate reached more than 96%. As shown in Fig. 9a, the possible

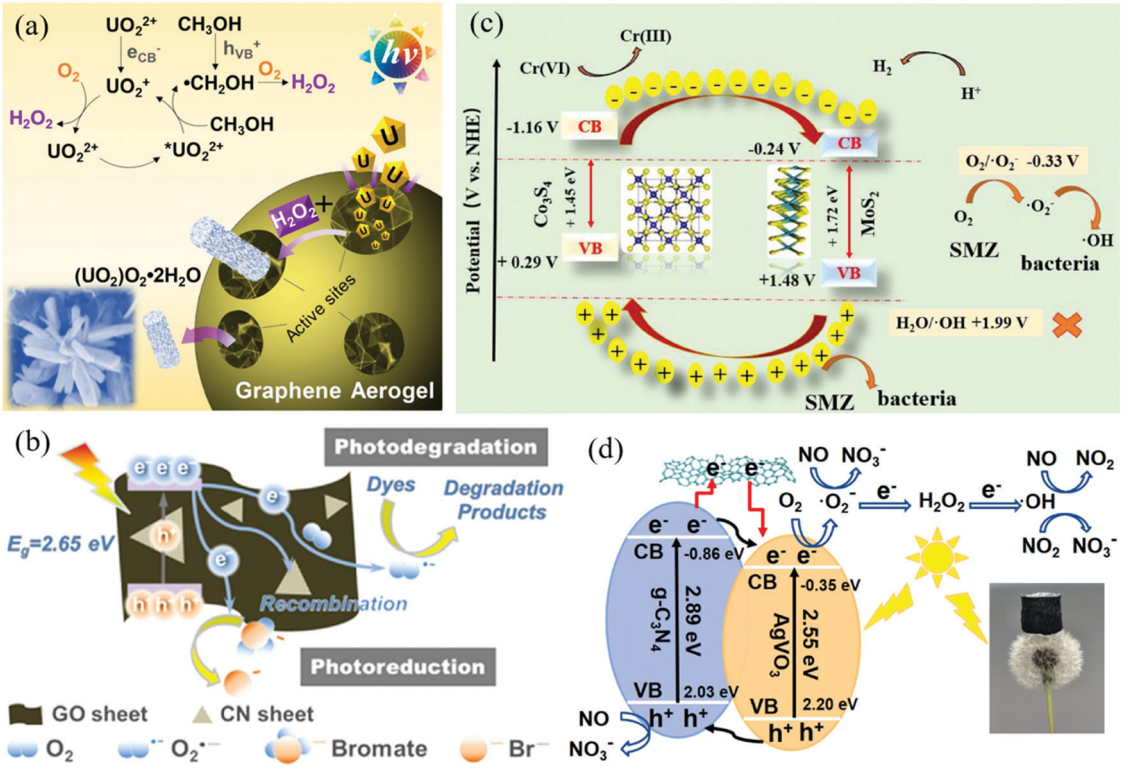


Fig. 9 Photocatalytic removal of pollutants with 2DM aerogels: (a) Schematic diagram of the principle of photocatalytic extraction of uranium by graphene aerogel under visible light irradiation and air atmosphere.[168] Copyright 2020, Elsevier. (b) Schematic diagram of photocatalytic degradation of g-$C_3N_4$/GO aerogel hybrid materials under visible light irradiation.[169] Copyright 2017, Elsevier. (c) The photocatalytic mechanism of $MoS_2$@$Co_3S_4$/nanofiber aerogel ($MoS_2$@$Co_3S_4$/NFA).[24] Copyright 2019, Elsevier. (d) The mechanism of photocatalytic removal of NO by $AgVO_3$-*g*-$C_3N_4$–graphene aerogel (AVO-CN-GA).[176] Copyright 2019, Elsevier.

mechanism of uranium removal is that the aggregated uranyl ions react with $H_2O_2$ in $N_2$ atmosphere to form ($UO_2$) $O_2{\cdot}2H_2O$ instead of $UO_2$. The efficient removal of uranium by GA-200 is due to the fact that the partially reduced GA retains certain functional groups, has a higher photocurrent response and a narrow band gap, and is easy to generate and transfer electrons/holes, which is conducive to the improvement of photocatalytic activity.

**6.2.2. Photocatalytic degradation of organic pollutants in water.** 2DM aerogels have good photocatalytic properties for anionic and cationic dyes, such as MO, MB, and RhB. Wu *et al.* reported a compressible and recyclable g-$C_3N_4$/GO aerogel hybrid material used as a visible light catalyst.[169] GO and g-$C_3N_4$ are closely bonded by the interaction of π–π stacking and hydrogen bonding, which makes the structure of hybrid materials more stable and provides a transmission channel for photoinduced electrons, benefiting for the separation of photogenerated carriers. The degradation rate of MO and MB reached 90% within 40 min. The degradation mechanism is shown in Fig. 9b, and the photocatalytic performance of the hybrid material is almost not decreased after continuous degradation for 5 times. The recyclability and sustainable utilization properties provide a potential possibility for practical application of g-$C_3N_4$/GO aerogel hybrid materials. Chen *et al.* used liquid phase exfoliation method to peel $WSe_2$, $WS_2$, $MoSe_2$, $MoS_2$ and other TMD materials into thin layers in water.[170] The photocatalytic activity of exfoliated TMDs such as $MoS_2$, $WS_2$, $MoSe_2$ and $WSe_2$ for MB dye was generally poor (the degradation rate of MB by $MoS_2$ sheet is only 15.15%). In order to further improve the adsorption and photocatalytic performance of $MoS_2$ nanosheets, 3D $MoS_2$ aerogels were prepared. After 20 min, the photocatalytic degradation of MB dyes by 3D $MoS_2$ aerogels reached 80%, which was greatly improved compared with $MoS_2$ nanosheets. Li and colleagues for the first time prepared nanorod-nanoflake $Nb_2O_5$-g-$C_3N_4$ (NbNR-CN) heterojunction by simple grinding and calcination, and then loaded NbNR-CN heterojunction on rGA to prepare 3D composite NbNR-CN/rGA.[171] $Nb_2O_5$ is a kind of wide band gap semiconductor material which responds to ultraviolet light. After forming NbNR-CN heterostructure, it has excellent visible light response. Combined with the high adsorption and conductivity of rGA, the photocatalytic degradation rate of RhB by NbNR-CN/rGA reached 94.8% within 100 min. Guan *et al.* synthesized direct Z-shaped g-$C_3N_4$-ZnO@GA (g-$C_3N_4$-ZnO@GA) heterostructures through hydrothermal self-assembly and freeze-drying.[172] The heterojunction preserved high catalytic activity of ZnO and g-$C_3N_4$, and showed good decomposition efficiency of RhB under ultraviolet and visible light, reaching 81.0% and 82.7% respectively, Also, the heterojunction has excellent reusable performance under the influence of porous hierarchical structure.

 

In addition to dyes, 2DM aerogels can also catalyze the degradation of organic compounds under visible light. For instance, Qiu *et al.* synthesized a new type of composite photocatalyst $MoS_2$@$Co_3S_4$/NFA supported on nanofiber aerogel (NFA) by solvothermal method.[24] NFA is composed of functionalized polyacrylonitrile (PAN) nanofibers interacting with hydrogen bonds and carbon nanofibers (CNFs). A unique core–shell heterostructure $MoS_2$@$Co_3S_4$ was constructed by the double template method. ZIF-67 was grown *in situ* on the surface of the first step template NFA, then NFA loaded with ZIF-67 was used as the second step template for the self-assembly of $MoS_2$, and ZIF-67 was converted into $Co_3S_4$ in the hydrothermal reaction. $MoS_2$@$Co_3S_4$/NFA with unique core–shell heterostructure showed excellent photocatalytic activity against typical pollutants (sulfamethoxazole and bacteria). The degradation mechanism is shown in Fig. 9c. The Z-type heterojunction structure can carry out different reactions on different photocatalysts in the system, which slows down the rapid recombination of photogenerated carriers and improves the service life of the photocatalyst. Luo's group chose to load bismuth sulfide ($Bi_2S_3$) and bismuth vanadate ($BiVO_4$) on the surface of GA to form a 3D all-solid Z-type heterojunction photocatalytic system (SVGA).[173] It was proved that $Bi_2S_3$ and $BiVO_4$ had matching heterostructure energy bands, thereby the photocatalytic activity of SVGA was improved. Under visible light irradiation, the removal rates of Cr(VI) and bisphenol A (BPA) by SVGA were close to 100% (after adsorption of 40 min and photocatalysis of 120 min). Gong and colleagues synthesized 3D graphene composite aerogel TA–$TiO_2$–GA with *in situ* growth of $TiO_2$ NPs by one-pot hydrothermal method and freeze-drying using tannic acid (TA) as reducing agent and cross-linking agent.[174] The obtained aerogel showed good photocatalytic activity for tetracycline (the removal rate reached 43.2%) and good reusability.

**6.2.3. Photocatalytic degradation of air pollutants.** 2DM aerogels as photocatalysts can not only be used to degrade pollutants in solution, but also remove pollutants from the air. The main research focuses on the catalytic conversion of NO, $CO_2$, and VOC by 2DM aerogels. In order to overcome the problems of poor electrical conductivity, small specific surface area and low absorption efficiency of visible light of g-$C_3N_4$, Lu *et al.* converted 2D g-$C_3N_4$ into 0D g-$C_3N_4$ quantum dots (CNQDs),[175] in which the CNQDs with a diameter of about 3 nm was uniformly modified on the surface of GO by hydrothermal method, and then tightly wrapped around the newly formed cube $InVO_4$ to form a 3D heterostructure CNQDs/GO-$InVO_4$ aerogel immediately. The formed aerogel had a photocatalytic efficiency of 65% for NO under visible light irradiation, and still had a strong photocatalytic effect on ppb grade (600 Ppb) NO, which is mainly due to the 3D interconnected layered structure of CNQDs/GO-$InVO_4$ aerogel and the synergistic effect of various substances. In a further study, they continued the strategy of previous work by modifying 2D g-$C_3N_4$ nanowires with 0D silver metavanadate ($AgVO_3$) quantum dots.[176] The resultant 0D-2D $AgVO_3$-*g*-$C_3N_4$ (marked as AVO-CN) heterojunction self-assembled with GO to form hydrogels and freeze-dried to obtain $AgVO_3$-*g*-$C_3N_4$-graphene aerogels (AVO-CN-GA). AVO-CN heterojunction and porous GO framework promote the separation of electron–hole pairs, endowing the AVO-CN-GA with excellent catalytic activity for the removal of NO (up to 65%), and have a strong photocatalytic effect on ppb (600 ppb) NO. The mechanism is shown in Fig. 9d.

Jung *et al.* synthesized a graphene aerogel loaded with mesoporous $TiO_2$ and multilayer $MoS_2$ by a simple one-pot hydrothermal method.[177] Due to the synergistic effect of the hierarchical porous structure and the three components, the photocatalytic reduction rate of the aerogel for $CO_2$ reached 92.33 mol CO per g $h^{-1}$. The electron flow from $TiO_2$ through

Table 4 Photocatalytic degradation of pollutants with 2DM aerogel photocatalysts

| 2DM-based aerogel photocatalysts | Pollutants (mg $L^{-1}$) | Light source (W) | $\lambda$ (nm) | Degradation rate (time, min) | Ref. |
|---|---|---|---|---|---|
| g-$C_3N_4$@cellulose aerogel/blended polyester fibers | Sulfaquinoxaline, Cr(VI) | Artificial solar light | — | Sulfaquinoxaline: 100% (60) Cr(VI): 97% (120) | 27 |
| $MoS_2$/RGO | Cr(VI) | Xe lamp (300) | >420 | 92% (120) | 166 |
| $C_3N_5$/RGO | Uranium(VI) | Xe lamp (300) | >420 | 94.9% | 167 |
| Graphene | Uranyl | Xe lamp (350) | >420 | 96% (60) | 168 |
| g-$C_3N_4$/GO | MB and MO (20), bromate (0.25) | Xe lamp (300) | >420 | MB and MO: ~90% (40), bromate: 80% (60) | 169 |
| $MoS_2$ | MB (50) | Xe lamp (300) | >420 | 80% (550) | 170 |
| $Nb_2O_5$-*g*-$C_3N_4$/RGO | RhB (20) | Xe lamp (300) | >420 | 94.8% (100) | 171 |
| g-$C_3N_4$-ZnO@ graphene | RhB (20) | Xe lamp (300) | >420, <380 | >420 nm: 81.0% (30) <380 nm: 82.7% (30) | 172 |
| $MoS_2$@$Co_3S_4$/nanofiber | Cr(VI) (10), sulfamethoxazole (20), and bacteria | Xe lamp (500) | — | Cr(VI): 90% (50) | 24 |
| $Bi_2S_3$-$BiVO_4$–graphene | Cr(VI) (50) and BPA (10) | Xe lamp (300) | >420 | Cr(VI) and BPA: 100% (120) | 173 |
| TA-$TiO_2$–graphene | Tetracycline (10), MB (10) and RhB (10) | Xe lamp (300) | >420 | Tetracycline: 43.2% (180) MB: 77.8% (180) RhB: 91.9% (180) | 174 |
| g-$C_3N_4$ quantum dots/ graphene–$InVO_4$ | NO | Xe lamp (300) | >420 | 65% (10) | 175 |
| $AgVO_3$-*g*-$C_3N_4$–graphene | NO | Xe lamp (300) | >420 | 65% (30) | 176 |
| $TiO_2$–$MoS_2$–graphene | $CO_2$ | Xe lamp (300) | >420 | 97% | 177 |
| g-$C_3N_4$/GO | MO (20) and $CO_2$ | Xe lamp (500) | >420 | MO: 92% (240) | 178 |

graphene to several layers of $MoS_2$ can effectively reduce the charge recombination rate and increase the reduction rate of $CO_2$. Jiang and colleagues reported a 3D porous g-$C_3N_4$/graphene oxide aerogel (CNGA) synthesized by hydrothermal self-assembly.[178] Thanks to the increase of active center and electron transfer rate at the large plane interface between g-$C_3N_4$ and GO nanosheets, the removal rate of MO by CNGA was as high as 92% within 4 hours. Not only that, CNGA can also reduce $CO_2$, one of the decomposition products of MO, to CO with a yield of 23 mmol $g^{-1}$ (within 6 hours), all of which are far ultra-pure g-$C_3N_4$.

The above introduction on photocatalytic degradation of pollutants with 2DM aerogels are summarized in Table 4.

### 6.3. Sterilization

Bacteria are one of the main causes of wound infections and diseases that endanger human health. 2DM aerogel proved to be a potentially good sterilizing material. Using natural biomass sucrose as a carbon source, Bajpai *et al.* synthesized GA with the 3D connected microporous structure by one-step pyrolysis.[179] GA showed good biocompatibility and was able to completely adsorb Staphylococcus aureus (a food contaminant

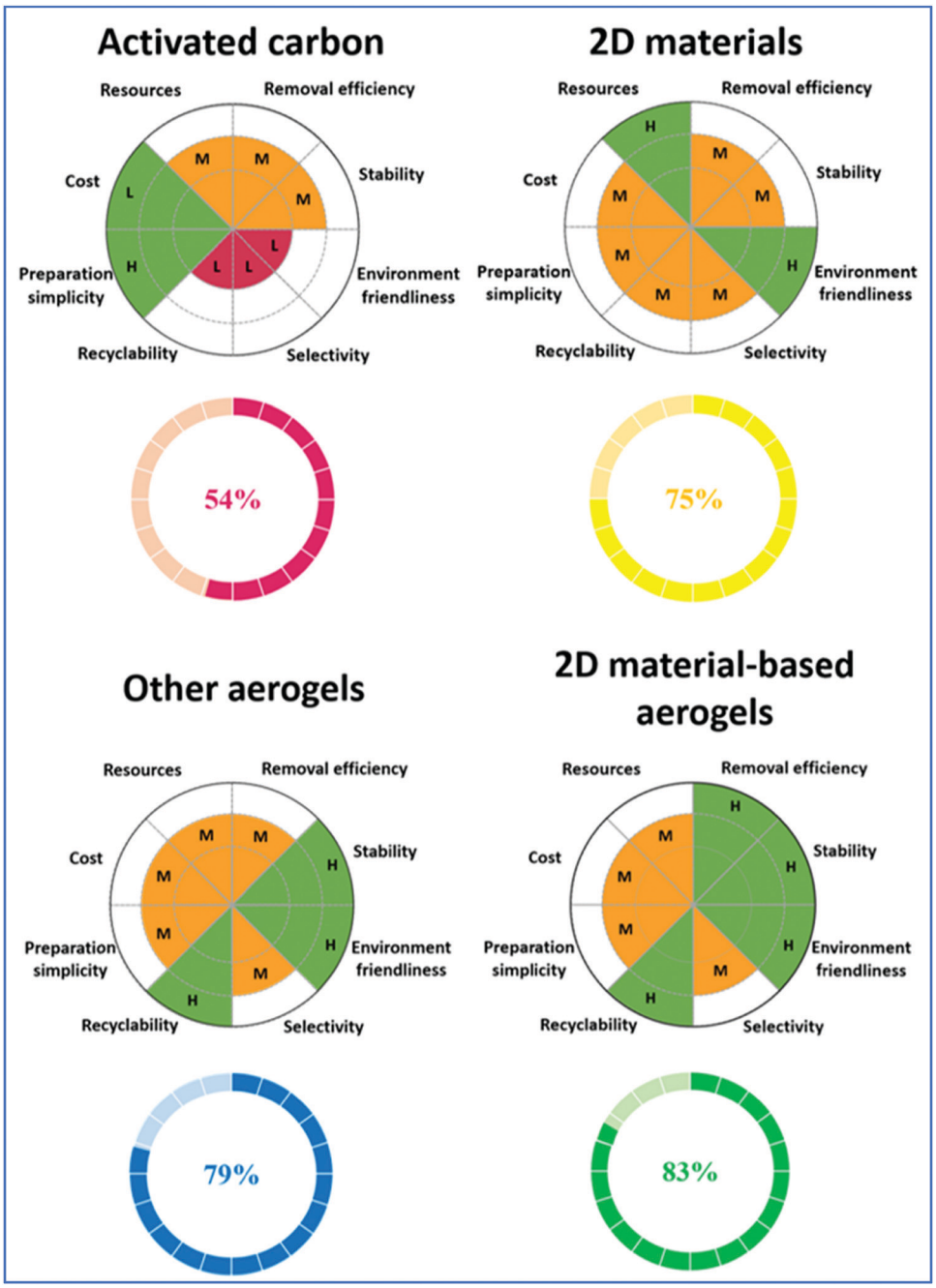


Fig. 10 The sustainability analysis of 2DM-based aerogels by comparing with activated carbon, 2DMs, and other aerogels *via* the Sustainability Footprint method.



 

and cause poor wound healing) within 80 min. Furthermore, GA also has good adsorption capacity for histamine, body amine and spermidine in actual soy sauce samples, and is an ideal food sterilization material. Liu *et al.* prepared Ag NPs-loaded N-doped 3D graphene aerogels (N-GA/Ag) by a one-step hydrothermal method.[180] The doping of N atoms promoted the dispersion of Ag NPs attached to the GO sheets, and the resulting Ag NPs were 10-50 nm in size. The composite aerogel showed good bactericidal efficiency against Gram-negative Escherichia coli (up to 100% within 24 h). Jiang *et al.* reported B and N co-doped graphene aerogels (BNGAs).[181] B and N are doping into the honeycomb framework of GA in a unique molecular configuration. Therefore, BNGAs, as photocatalysts, showed a good purification function for water contaminated by pathogenic bacteria such as Escherichia coli, with a bactericidal rate of $1.2 \times 10^3$ CFU $h^{-1}$ $g_{cat}^{-1}$.

## 7. Sustainability analysis

In the field of environmental monitoring and remediation, in order to avoid secondary pollution to the environment, the environmental friendliness and sustainable utilization of the materials used are particularly important. In this part, we use the Sustainability Footprint (SF) method developed by Mezzenga *et al.* to assess the sustainability of 2DM-based aerogels in the field of adsorption.[182,183] We compared the sustainability of traditional adsorbent activated carbon, 2D materials, and 2DM-based aerogels. As shown in Fig. 10, the sustainability of 2DM-based aerogel is analyzed mainly by considering eight sustainable development factors, including the removal efficiency, stability, environmental friendliness, selectivity, recyclability, preparation simplicity, cost, and resources. The overall sustainable footprint (OSF) value can be calculated according to the following formula:

$$\mathrm{OSF} = 100\% \times \sum_{j=1}^{8} \left(\frac{i}{3}\right)_j \times \frac{1}{8}$$

Among them, "*j*" represents eight sustainable development factors, and "*i*" represents the score of each factor, which are low ($i = 1$), medium ($i = 2$), and high ($i = 3$). Since the "cost" factor is a negative factor affecting sustainability, low cost will be assigned a value of $i = 3$, and high cost will be assigned a value of $i = 1$.

The results obtained after SF analysis indicate that activated carbon is the worst sustainable adsorbent, mainly because it has a negative impact on the environment, and it also performs poorly in terms of selectivity and recyclability. Compared with activated carbon, 2DMs have improved environmental friendliness, selectivity, and reproducibility, but their adsorption performance is not good. Compared with the former, the stability and recyclability of aerogels outside of 2DM are greatly improved. 2DM-based aerogels not only have better environmental friendliness, selectivity, and reproducibility, but also have extremely high adsorption efficiency for various pollutants. After calculation, the OSF values of activated carbon, 2DMs, other non-2DM aerogels, and 2DM-based aerogel are 54%, 75%, 79%, and 83%, respectively. Based on the sustainability analysis of various materials, we suggest that 2DM-based aerogels have better sustainable performance than other types of materials.

## 8. Conclusion and outlooks

In summary, we provide a comprehensive and systematic overview of the synthesis, function tailoring, and environmental applications of 2DM-based aerogels. By selecting and designing appropriate methods and using the ice template method, the structure and function of the 2DM-based aerogel can be microregulated, thereby synthesizing environmentally friendly aerogels with high mechanical strength, specific surface area and porosity. In addition, the 3D macroporous structure of aerogel can also be used as a carrier for many dopants to add additional physical and chemical properties to meet the needs of actual environmental applications. Therefore, the 2DM-based aerogels are excellent materials for the detection and treatment of gaseous pollutants, organic and inorganic pollutants in water and air systems.

However, 2DM-based aerogels for environmental detection and remediation applications still have certain problems, and studies for solving these problems are expected to be a breakthrough point for widespread applications in the future. It is expected that 2DM aerogels are utilized to achieve large-scale industrialization and commercialization in the future, which can effectively improve the living environment of the existing human society. First of all, in terms of synthesis process, both supercritical drying and freeze-drying technologies have problems such as long cycle, high threshold, large energy consumption, complicated operation and easy to cause secondary pollution. Atmospheric drying technology is the key to the large-scale industrial production of aerogels, and further enhances the mechanical strength of the aerogel network to prevent the gel network from collapsing under atmospheric drying. Secondly, both 2DMs and 2DM-based precursors are expensive. How to synthesize 2DMs and their 2DM aerogels from cheap and environmentally friendly raw materials (natural minerals or biomass raw materials) is also one of the future research trends. At present, the 2DMs used for the developed 2DM-based aerogels are still too limited. The 2DM family has many members. The development of 2D covalent organic framework (COF)- and MOF-based aerogels will also become one of the hottest topics in the future. Third, in terms of environmental monitoring, the colorimetric sensing based on 2DM aerogels is a simple and fast monitoring method. The monitoring of bacteria and viruses in foods can effectively protect human health. Fourth, in terms of environmental remediation, 2DM aerogels are expected to demonstrate their unique capabilities in the field of high-efficiency elimination of air pollutants (especially VOCs and bacteria) and anionic pollutants. The development of 2DM-based aerogels with novel heterojunction structures is also one of the potential strategies to solve the low efficiency of photocatalytic degradation of pollutants. Finally, the development and manufacture of 2DM aerogels with high elasticity and mechanical strength is also one of the effective means to increase the recycling ability and reduce the cost.

It should be noted that the materials informatics is the application of emerging technologies such as data science, internet, computer science, and engineering in materials science and engineering to accelerate material innovation.[184–186] In the future, materials informatics is expected to guide the design, synthesis, and even industrial production of more novel 2DM aerogels. On the basis of computer simulation and machine learning, the most suitable 2DM aerogels for environmental science applications could be screened by referring to the material database. In addition, the materials informatics will be helpful to improve the material efficiency in industrial manufacturing and to design optimal routes for material synthesis.

## Abbreviation

| | |
|---|---|
| TMB | 3,3',5,5'-Tetramethylbenzidine |
| PEDOT | 3,4-Ethylenedioxythiophene |
| GPTMS | 3-Glycidoxypropyl trimethoxysilane |
| APT | Acetamiprid aptamer |
| AFB1 | Aflatoxin B1 |
| ANF | Aramid nanofiber |
| BC | Bacterial nanocellulose |
| BP | Black phosphorus |
| BNNR | Boron nitride nanoribbon |
| BNNS | Boron nitride nanosheet |
| CA | Calcium alginate |
| CDM | Carbendazim |
| CILE | Carbon ionic liquid electrode |
| CNTs | Carbon nanotubes |
| CN | Carbon nitride |
| CQD | Carbon quantum dot |
| CMC | Carboxymethyl cellulose |
| CNF | Cellulose nanofiber |
| CS | Chitosan |
| Dcp | Dichlorophenol |
| DMDMS | Dimethoxydimethylsilane |
| DIW | Direct ink writing |
| f-NCC | Functionalized nanocellulose |
| GC-NPD | Gas chromatography-nitrogen phosphorous detection |
| CNN | g-$C_3N_4$ nanosheet |
| CNQD | g-$C_3N_4$ quantum dot |
| GA | Graphene aerogel |
| GHB | Graphene hydrogel block |
| GO | Graphene oxide |
| GONR | Graphene oxide nanoribbon |
| GS | Graphene sheet |
| g-$C_3N_4$ | Graphitic carbon nitride |
| h-BN | Hexagonal boron nitride |
| HIPE | High internal phase emulsion |
| LDH | Layered double hydroxide |
| LC | Liquid crystal |
| MCNS | Magnetic carbon nanospheres |
| MSPE | Magnetic solid phase extraction |
| MNPs | Metal nanoparticles |
| MOF | Metal organic frame |
| MOA | Metal organic aerogel |
| MO | Methyl orange |
| MB | Methylene blue |
| MMO | Mixed metal oxide |
| MNS | $MnO_2$ nanosheet |
| MWCNT | Multi-walled carbon nanotube |
| MXSs | MXene-surfactants |
| NFA | Nanofiber aerogel |
| NPs | Nanoparticles |
| NGA | N-Doped graphene aerogel |
| OPP | Organophosphorus pesticide |
| OSF | Overall sustainable footprint |
| PAN | Polyacrylonitrile |
| PDMS | Polydimethylsiloxane |
| PDA | Polydopamine |
| PI | Polyimide |
| PPy | Polypyrrole |
| PS | Polystyrene |
| PVA | Polyvinyl alcohol |
| PVP | Polyvinylpyrrolidone |
| PB | Prussian blue |
| PBA | Prussian blue analogue |
| PEDOT: PSS | 3-ethylenedioxythiophene: polystyrene sulfonate |
| RGO | Reduced graphene oxide |
| RGA | Reduced graphene oxide aerogel |
| RF | Resorcinol-formaldehyde |
| R6G | Rhodamine 6G |
| RhB | Rhodamine B |
| RDE | Rotating disk electrode |
| ssDNA | Single-strand DNA |
| SA | Sodium alginate |
| SERS | Surface enhanced Raman scattering |
| SPR | Surface plasmon resonance |
| SF | Sustainability footprint |
| TA | Tannic acid |
| 3D | Three-dimensional |
| TMD | Transition metal dichalcogenide |
| TMO | Transition metal oxides |
| TMP | Transition metal phosphide |
| MTMS | Trimethoxymethylsilane |
| 2DM | Two-dimensional material |
| VOC | Volatile organic compound |
| ZIF-8 | Zeolite imidazole framework-8 |
| β-CD | β-Cyclodextrin. |

## Conflicts of interest

The authors declare no conflict of interests.

## Acknowledgements

The authors thank the financial support from the National Natural Science Foundation of China (No. 51873225), the Taishan

 

Scholars Program of Shandong Province (No. tsqn201909104), and the High-Grade Talents Plan of Qingdao University.

## References

1 S. Rajagopaslan, G. Al-Kindi Sadeer and D. Brook Robert, *J. Am. Coll. Cardiol.*, 2018, **72**, 2054–2070.
2 A. Y. Hoekstra, J. Buurman and K. C. H. van Ginkel, *Environ. Res. Lett.*, 2018, **13**, 053002.
3 B. Liu, J. Y. Zhuang and G. Wei, *Environ. Sci.: Nano*, 2020, **7**, 2195–2213.
4 D. Z. Zhu, B. Liu and G. Wei, *Biosensors*, 2021, **11**, 259.
5 V. Georgakilas, J. N. Tiwari, K. C. Kemp, J. A. Perman, A. B. Bourlinos, K. S. Kim and R. Zboril, *Chem. Rev.*, 2016, **116**, 5464–5519.
6 H. M. Wang, C. H. Li, P. F. Fang, Z. L. Zhang and J. Z. Zhang, *Chem. Soc. Rev.*, 2018, **47**, 6101–6127.
7 L. Yang, Y. T. Peng, X. D. Luo, Y. Dan, J. H. Ye, Y. Zhou and Z. G. Zou, *Chem. Soc. Rev.*, 2021, **50**, 2147–2172.
8 M. M. Hu, H. Zhang, T. Hu, B. B. Fan, X. H. Wang and Z. J. Li, *Chem. Soc. Rev.*, 2020, **49**, 6666–6693.
9 S. Roy, X. Zhang, A. B. Puthirath, A. Meiyazhagan, S. Bhattacharyya, M. M. Rahman, G. Babu, S. Susarla, S. K. Saju, M. K. Tran, L. M. Sassi, M. A. S. R. Saadi, J. W. Lai, O. Sahin, S. M. Sajadi, B. Dharmarajan, D. Salpekar, N. Chakingal, A. Baburaj, X. T. Shuai, A. Adumbumkulath, K. A. Miller, J. M. Gayle, A. Ajnsztajn, T. Prasankumar, V. V. J. Harikrishnan, V. Ojha, H. Kannan, A. Z. Khater, Z. W. Zhu, S. A. Iyengar, P. A. D. Autreto, E. F. Oliveira, G. H. Gao, A. G. Birdwell, M. R. Neupane, T. G. Ivanov, J. Taha-Tijerina, R. M. Yadav, S. Arepalli, R. Vajtai and P. M. Ajayan, *Adv. Mater.*, 2021, **33**, 2101589.
10 M. L. Pan, C. Shan, X. L. Zhang, Y. Y. Zhang, C. Y. Zhu, G. D. Gao and B. C. Pan, *Environ. Sci. Technol.*, 2018, **52**, 739–746.
11 L. Tan, C. F. Yu, M. Wang, S. Y. Zhang, J. Y. Sun, S. Y. Dong and J. H. Sun, *Appl. Surf. Sci.*, 2019, **467–468**, 286–292.
12 N. N. Wang, H. Wang, Y. Y. Wang, Y. H. Wei, J. Y. Si, A. C. Y. Yuen, J. S. Xie, B. Yu, S. E. Zhu, H. D. Lu, W. Yang, Q. N. Chan and G. H. Yeoh, *ACS Appl. Mater. Interfaces*, 2019, **11**, 40512–40523.
13 M. G. Chen, J. W. Xie, C. G. Xiong and H. Wang, *Ceram. Int.*, 2021, **47**, 19970–19977.
14 S. Nardecchia, D. Carriazo, M. L. Ferrer, M. C. Gutiérrez and F. del Monte, *Chem. Soc. Rev.*, 2013, **42**, 794–830.
15 G. Wei, J. M. Zhang, M. Usuelli, X. F. Zhang, B. Liu and R. Mezzenga, *Prog. Mater. Sci.*, 2022, **125**, 100915.
16 F. W. Wu, D. Liu, G. Y. Li, L. Q. Li, L. F. Yan, G. Hong and X. T. Zhang, *Nanoscale*, 2021, **13**, 5419–5428.
17 W. J. Liu, J. Y. Cai and Z. H. Li, *ACS Sustainable Chem. Eng.*, 2015, **3**, 277–282.
18 S. Zhou, W. Jiang, T. H. Wang and Y. Lu, *Ind. Eng. Chem. Res.*, 2015, **54**, 5460–5467.
19 Q. Dong, J. Wang, X. G. Duan, X. Y. Tan, S. M. Liu and S. B. Wang, *Chem. Eng. J.*, 2019, **369**, 1049–1058.
20 P. S. He, X. W. Tang, L. Chen, P. W. Xie, L. He, H. Zhou, D. Zhang and T. X. Fan, *Adv. Funct. Mater.*, 2018, **28**, 1801121.
21 M. Yang, N. F. Zhao, Y. Cui, W. W. Gao, Q. Zhao, C. Gao, H. Bai and T. Xie, *ACS Nano*, 2017, **11**, 6817–6824.
22 Y. S. Song, Y. S. Peng, N. V. Long, Z. R. Huang and Y. Yang, *Appl. Surf. Sci.*, 2021, **542**, 148584.
23 M. Liu, Z. Y. Wang, P. Song, Z. X. Yang and Q. Wang, *Sens. Actuators, B*, 2021, **340**, 129946.
24 J. L. Qiu, W. T. Zheng, R. R. Yuan, C. L. Yue, D. W. Li, F. Q. Liu and J. J. Zhu, *Appl. Catal., B*, 2020, **264**, 118514.
25 W. C. Wan, R. Y. Zhang, W. Li, H. Liu, Y. H. Lin, L. N. Li and Y. Zhou, *Environ. Sci.: Nano*, 2016, **3**, 107–113.
26 J. Liu, H. Wang, J. W. Bai, T. R. Li, Y. M. Yang, Y. Peng and B. D. Wang, *J. Mater. Chem. A*, 2017, **5**, 24920–24928.
27 S. J. Chen, W. Y. Lu, J. L. Han, H. T. Zhong, T. F. Xu, G. Q. Wang and W. X. Chen, *Chem. Eng. J.*, 2019, **359**, 119–129.
28 K. Q. Lu, X. Xin, N. Zhang, Z. R. Tang and Y. J. Xu, *J. Mater. Chem. A*, 2018, **6**, 4590–4604.
29 V. Chabot, D. Higgins, A. P. Yu, X. C. Xiao, Z. W. Chen and J. J. Zhang, *Energy Environ. Sci.*, 2014, **7**, 1564–1596.
30 S. B. Wang, H. Q. Sun, H. M. Ang and M. O. Tadé, *Chem. Eng. J.*, 2013, **226**, 336–347.
31 M. J. Lü, J. Li, X. Y. Yang, C. A. Zhang, J. Yang, H. Hu and X. B. Wang, *Chin. Sci. Bull.*, 2013, **58**, 2698–2710.
32 H. Maleki, *Chem. Eng. J.*, 2016, **300**, 98–118.
33 K. J. Yang, J. Wang, X. X. Chen, Q. Zhao, A. Ghaffar and B. L. Chen, *Environ. Sci.: Nano*, 2018, **5**, 1264–1297.
34 Y. Shen, Q. L. Fang and B. L. Chen, *Environ. Sci. Technol.*, 2015, **49**, 67–84.
35 K. C. Lai, L. Y. Lee, B. Y. Z. Hiew, S. Thangalazhy-Gopakumar and S. Y. Gan, *J. Environ. Sci.*, 2019, **79**, 174–199.
36 Y. Z. Zhang, J. K. El-Demellawi, Q. Jiang, G. Ge, H. F. Liang, K. Lee, X. C. Dong and H. N. Alshareef, *Chem. Soc. Rev.*, 2020, **49**, 7229–7251.
37 M. A. Worsley, P. J. Pauzauskie, T. Y. Olson, J. Biener, J. H. Satcher and T. F. Baumann, *J. Am. Chem. Soc.*, 2010, **132**, 14067–14069.
38 H. S. Yang, Z. L. Li, B. Lu, J. Gao, X. T. Jin, G. Q. Sun, G. F. Zhang, P. P. Zhang and L. T. Qu, *ACS Nano*, 2018, **12**, 11407–11416.
39 N. F. Hasmuni, S. Ismail, A. Z. A. Kadir, I. Sudin, M. Aziz and M. Z. M. Yusop, *AIP Conf. Proc.*, 2019, **2068**, 020111.
40 S. Yan, G. Z. Zhang, F. B. Li, L. Zhang, S. T. Wang, H. H. Zhao, Q. Ge and H. J. Li, *Nanoscale*, 2019, **11**, 10372–10380.
41 H. S. Yang, T. P. Zhang, M. Jiang, Y. X. Duan and J. M. Zhang, *J. Mater. Chem. A*, 2015, **3**, 19268–19272.
42 W. W. Zhan, S. R. Yu, L. Gao, F. Wang, X. Fu, G. Sui and X. P. Yang, *ACS Appl. Mater. Interfaces*, 2018, **10**, 1093–1103.
43 J. Luo, J. P. Lai, N. Zhang, Y. B. Liu, R. Liu and X. Y. Liu, *ACS Sustainable Chem. Eng.*, 2016, **4**, 1404–1413.
44 Y. L. He, J. H. Li, L. F. Li and J. Y. Li, *Mater. Lett.*, 2016, **177**, 76–79.
45 S. L. Wang, R. H. Wang, Q. N. Zhao, L. Ren, J. Wen, J. Chang, X. L. Fang, N. Hu and C. H. Xu, *J. Colloid Interface Sci.*, 2019, **544**, 37–45.

46 S. W. Shi, B. Q. Qian, X. Y. Wu, H. L. Sun, H. Q. Wang, H. B. Zhang, Z. Z. Yu and T. P. Russell, *Angew. Chem., Int. Ed.*, 2019, **58**, 18171–18176.
47 H. H. Ou, P. J. Yang, L. H. Lin, M. Anpo and X. C. Wang, *Angew. Chem., Int. Ed.*, 2017, **56**, 10905–10910.
48 J. M. Jeong, M. H. Yang, D. S. Kim, T. J. Lee, B. G. Choi and D. H. Kim, *J. Colloid Interface Sci.*, 2017, **506**, 379–385.
49 Y. M. Zhang, F. Wang, D. D. Zhang, J. Chen, H. Zhu, L. C. Zhou and Z. Chen, *Mater. Lett.*, 2017, **208**, 73–76.
50 J. Z. Feng, B. L. Su, H. S. Xia, S. Y. Zhao, C. Gao, L. K. Wang, O. Ogbeide, J. Feng and T. Hasan, *Chem. Soc. Rev.*, 2021, **50**, 3842–3888.
51 C. Zhu, T. Y. J. Han, E. B. Duoss, A. M. Golobic, J. D. Kuntz, C. M. Spadaccini and M. A. Worsley, *Nat. Commun.*, 2015, **6**, 6962.
52 Q. Q. Zhang, F. Zhang, S. P. Medarametla, H. Li, C. Zhou and D. Lin, *Small*, 2016, **12**, 1702–1708.
53 O. Guler, S. H. Guler and M. Taskin, *Bull. Mater. Sci.*, 2019, **42**, 7.
54 Z. Xu, Y. Zhang, P. G. Li and C. Gao, *ACS Nano*, 2012, **6**, 7103–7113.
55 J. Y. Hong, E. H. Sohn, S. Park and H. S. Park, *Chem. Eng. J.*, 2015, **269**, 229–235.
56 G. T. Fu, X. X. Yan, Y. F. Chen, L. Xu, D. M. Sun, J. M. Lee and Y. W. Tang, *Adv. Mater.*, 2018, **30**, 1704609.
57 Y. M. Huangfu, C. B. Liang, Y. X. Han, H. Qiu, P. Song, L. Wang, J. Kong and J. W. Gu, *Compos. Sci. Technol.*, 2019, **169**, 70–75.
58 C. L. Li, Q. Cao, F. Z. Wang, Y. Q. Xiao, Y. B. Li, J. J. Delaunay and H. W. Zhu, *Chem. Soc. Rev.*, 2018, **47**, 4981–5037.
59 M. J. Crane, M. B. Lim, X. Z. Zhou and P. J. Pauzauskie, *Microsyst. Nanoeng.*, 2017, **3**, 17032.
60 Z. Y. Yang, P. Zhang, J. Wang, Y. Yan, Y. Yu, Q. H. Wang and M. K. Liu, *ACS Appl. Mater. Interfaces*, 2018, **10**, 37434–37444.
61 X. Zhang, J. Zhou, Y. Y. Zheng and D. Y. Chen, *J. Power Sources*, 2019, **439**, 227112.
62 D. Yuan, Y. H. Dou, Z. Z. Wu, Y. H. Tian, K. H. Ye, Z. Lin, S. X. Dou and S. Q. Zhang, *Chem. Rev.*, 2021, **122**, 957–999.
63 H. Zhang, Q. Qi, P. G. Zhang, W. Zheng, J. Chen, A. G. Zhou, W. B. Tian, W. Zhang and Z. M. Sun, *ACS Appl. Energy Mater.*, 2019, **2**, 705–714.
64 G. Y. Zhu, L. B. Ma, H. N. Lin, P. Y. Zhao, L. Wang, Y. Hu, R. P. Chen, T. Chen, Y. R. Wang, Z. X. Tie and Z. Jin, *Nano Res.*, 2019, **12**, 1713–1719.
65 J. Zhou, B. Y. Yan, J. Yang, Y. Yang, W. Zhou, H. Lan, H. Wang and L. Guo, *Nanoscale*, 2018, **10**, 9108–9114.
66 H. Li, X. L. Zhao, H. L. Liu, S. Chen, X. F. Yang, C. X. Lv, H. W. Zhang, X. L. She and D. J. Yang, *Small*, 2018, **14**, 1802824.
67 S. J. Lai, C. X. Lv, S. Chen, P. Lu, X. L. She, L. Wan, H. W. Wang, J. Sun, D. J. Yang and X. L. Zhao, *J. Alloys Compd.*, 2020, **817**, 152727.
68 Z. X. Zhou, Y. Y. Zhang, Y. F. Shen, S. Q. Liu and Y. J. Zhang, *Chem. Soc. Rev.*, 2018, **47**, 2298–2321.
69 H. J. Qi, X. D. Ji, C. Shi, R. X. Ma, Z. H. Huang, M. H. Guo, J. Li and Z. H. Guo, *J. Colloid Interface Sci.*, 2019, **556**, 366–375.
70 J. Q. Pan, B. B. Wang, Z. J. Dong, C. Zhao, Z. Y. Jiang, C. S. Song, J. J. Wang, Y. Y. Zheng and C. R. Li, *Int. J. Hydrogen Energy*, 2019, **44**, 19942–19952.
71 Y. Y. Liu, S. Y. Yang, S. N. Yin, L. G. Feng, Y. Zang and H. G. Xue, *Chem. Eng. J.*, 2018, **334**, 2401–2407.
72 C. R. McConnell and S. Y. Liu, *Chem. Soc. Rev.*, 2019, **48**, 3436–3453.
73 W. J. Wu, H. W. Liu, Z. Y. Wang, P. Lv, E. T. Hu, J. J. Zheng, K. H. Yu and W. Wei, *Ceram. Int.*, 2021, **47**, 33926–33929.
74 M. A. Kashfipour, R. S. Dent, N. Mehra, X. T. Yang, J. W. Gu and J. H. Zhu, *Compos. Sci. Technol.*, 2019, **182**, 107715.
75 G. Y. Li, M. Y. Zhu, W. B. Gong, R. Du, A. Eychmuller, T. T. Li, W. B. Lv and X. T. Zhang, *Adv. Funct. Mater.*, 2019, **29**, 1900188.
76 Z. H. Chen, Y. J. Hu, H. Zhuo, L. X. Liu, S. S. Jing, L. X. Zhong, X. W. Peng and R. C. Sun, *Chem. Mater.*, 2019, **31**, 3301–3312.
77 Z. H. Zhou, J. Z. Liu, X. X. Zhang, D. Tian, Z. Y. Zhan and C. H. Lu, *Adv. Mater. Interfaces*, 2019, **6**, 1802040.
78 L. Wang, M. Y. Zhang, B. Yang, J. J. Tan and X. Y. Ding, *ACS Nano*, 2020, **14**, 10633–10647.
79 L. P. Liao, A. T. Zhang, K. Zheng, R. Liu, Y. J. Cheng, L. H. Wang, A. H. Li and J. Q. Liu, *ACS Appl. Mater. Interfaces*, 2021, **13**, 28222–28230.
80 B. Liu, M. Jiang, D. Z. Zhu, J. M. Zhang and G. Wei, *Chem. Eng. J.*, 2022, **428**, 131118.
81 B. X. Zhang, J. L. Zhang, C. C. Liu, L. Peng, X. X. Sang, B. X. Han, X. Ma, T. Luo, X. N. Tan and G. Y. Yang, *Sci. Rep.*, 2016, **6**, 21401.
82 J. L. Zheng, X. Pan, X. M. Huang, D. B. Xiong, Y. Shang, X. X. Li, N. Wang, W. M. Lau and H. Y. Yang, *Chem. Eng. J.*, 2020, **396**, 125197.
83 X. W. Xu, H. Chu, Z. Q. Zhang, P. Dong, R. Baines, P. M. Ajayan, J. F. Shen and M. X. Ye, *ACS Appl. Mater. Interfaces*, 2017, **9**, 32756–32766.
84 M. Z. Yazdan-Abad, M. Noroozifar, A. R. M. Alam and H. Saravani, *J. Mater. Chem. A*, 2017, **5**, 10244–10249.
85 M. Z. Yazdan-Abad, M. Noroozifar, A. S. Douk, A. R. Modarresi-Alam and H. Saravani, *Appl. Catal., B*, 2019, **250**, 242–249.
86 C. Y. Xing, G. H. Jing, X. Liang, M. Qiu, Z. J. Li, R. Cao, X. J. Li, D. Y. Fan and H. Zhang, *Nanoscale*, 2017, **9**, 8096–8101.
87 X. S. Du, J. H. Qiu, S. Deng, Z. L. Du, X. Cheng and H. B. Wang, *J. Mater. Chem. A*, 2020, **8**, 14126–14134.
88 G. Q. Wang, S. H. Hou, C. Yan, Y. Lin and S. M. Liu, *Chem. Eng. J.*, 2017, **322**, 611–617.
89 X. C. Xiong, N. Ji, C. F. Song and Q. L. Liu, *Procedia Eng.*, 2015, **121**, 957–960.
90 H. X. Bei, R. Y. Li, Z. J. Li, J. K. Liu, Z. G. Gu and G. L. Wang, *RSC Adv.*, 2015, **5**, 54211–54219.
91 L. Lin, Q. Xie, M. J. Zhang, C. X. Liu, Y. S. Zhang, G. T. Wang, P. Zou, J. Zeng, H. Chen and M. J. Zhao, *Colloids Surf., A*, 2020, **601**, 124978.

 

92 L. Li, S. J. He, M. M. Liu, C. M. Zhang and W. Chen, *Anal. Chem.*, 2015, **87**, 1638–1645.
93 Y. Li, R. F. Zhang, X. K. Tian, C. Yang and Z. X. Zhou, *Appl. Surf. Sci.*, 2016, **369**, 11–18.
94 D. A. Reddy, J. Choi, S. Lee, R. Ma and T. K. Kim, *RSC Adv.*, 2015, **5**, 18342–18351.
95 H. J. He, L. H. Huang, Z. J. Zhong and S. Z. Tan, *Appl. Surf. Sci.*, 2018, **441**, 285–294.
96 W. W. Kang, Y. Cui, L. Qin, Y. Z. Yang, Z. B. Zhao, X. Z. Wang and X. G. Liu, *J. Hazard. Mater.*, 2020, **392**, 122499.
97 G. Z. Yang, H. Kong, Y. Chen, B. Liu, D. Z. Zhu, L. Guo and G. Wei, *Carbohydr. Polym.*, 2022, **279**, 118947.
98 J. J. Cao, Z. Y. Wang, X. H. Yang, J. Tu, R. L. Wu and W. Wang, *Appl. Surf. Sci.*, 2018, **444**, 399–406.
99 A. Krittayavathananon and M. Sawangphruk, *Anal. Chem.*, 2017, **89**, 13283–13289.
100 K. K. Wu, X. Y. Liu, Z. T. Li, Y. P. Jiao and C. R. Zhou, *Mater. Sci. Eng., C*, 2020, **106**, 110162.
101 E. P. Ferreira-Neto, S. Ullah, T. C. A. da Silva, R. R. Domeneguetti, A. P. Perissinotto, F. S. de Vicente, U. P. Rodrigues-Filho and S. J. L. Ribeiro, *ACS Appl. Mater. Interfaces*, 2020, **12**, 41627–41643.
102 T. M. Zhang, W. W. Zhang, H. Xi, Q. Q. Li, M. X. Shen, G. B. Ying and J. F. Zhang, *Cellulose*, 2021, **28**, 4281–4293.
103 Z. Zheng, Y. L. Zhao, J. H. Hu and H. T. Wang, *ACS Appl. Mater. Interfaces*, 2020, **12**, 47854–47864.
104 Q. Y. Tian, J. K. Xu, Y. X. Zuo, Y. Y. Li, J. L. Zhang, Y. Y. Zhou, X. M. Duan, L. M. Lu, H. Y. Jia, Q. Xu and Y. F. Yu, *J. Electroanal. Chem.*, 2019, **837**, 1–9.
105 A. Shahzad, M. Moztahida, K. Tahir, B. Kim, H. Jeon, A. A. Ghani, N. Maile, J. Jang and D. S. Lee, *J. Nucl. Mater.*, 2020, **539**, 152277.
106 M. Ikram, H. Lv, Z. Liu, M. Khan, L. J. Liu, F. Raziq, X. Bai, M. Ullah, Y. Zhang and K. Y. Shi, *Chem. Mater.*, 2020, **32**, 7215–7225.
107 H. Ryu, B. Li, S. De Guise, J. McCutcheon and Y. Lei, *J. Hazard. Mater.*, 2021, **408**, 124437.
108 T. Yang, R. Z. Yu, Y. H. Yan, H. Zeng, S. Z. Luo, N. Z. Liu, A. Morrin, X. L. Luo and W. H. Li, *Sens. Actuators, B*, 2018, **274**, 501–516.
109 L. H. Zhi, W. Zuo, F. J. Chen and B. D. Wang, *ACS Sustainable Chem. Eng.*, 2016, **4**, 3398–3408.
110 Y. J. Long, Y. F. Li, Y. Liu, J. J. Zheng, J. Tang and C. Z. Huang, *Chem. Commun.*, 2011, **47**, 11939–11941.
111 M. X. Lu, Y. J. Deng, Y. Luo, J. P. Lv, T. B. Li, J. Xu, S. W. Chen and J. Y. Wang, *Anal. Chem.*, 2019, **91**, 888–895.
112 X. Ma, F. Gao, G. B. Liu, Y. Xie, X. L. Tu, Y. Z. Li, R. Y. Dai, F. L. Qu, W. M. Wang and L. M. Lu, *Microchim. Acta*, 2019, **186**, 291.
113 Y. Xie, X. L. Tu, X. Ma, M. Q. Xiao, G. B. Liu, F. L. Qu, R. Y. Dai, L. M. Lu and W. M. Wang, *Electrochim. Acta*, 2019, **311**, 114–122.
114 T. Kokulnathan and S. M. Chen, *ACS Appl. Mater. Interfaces*, 2020, **12**, 16216–16226.
115 S. Mahpishanian and H. Sereshti, *J. Chromatogr. A*, 2016, **1443**, 43–53.
116 P. Wuamprakhon, A. Krittayavathananon, N. Ma, N. Phattharasupakun, T. Maihom, J. Limtrakul and M. Sawangphruk, *J. Electroanal. Chem.*, 2018, **808**, 124–132.
117 H. Long, A. Harley-Trochimczyk, T. Pham, Z. R. Tang, T. L. Shi, A. Zettl, C. Carraro, M. A. Worsley and R. Maboudian, *Adv. Funct. Mater.*, 2016, **26**, 5158–5165.
118 H. Long, L. Chan, A. Harley-Trochimczyk, L. E. Luna, Z. R. Tang, T. L. Shi, A. Zettl, C. Carraro, M. A. Worsley and R. Maboudian, *Adv. Mater. Interfaces*, 2017, **4**, 1700217.
119 W. J. Yan, A. Harley-Trochimczyk, H. Long, L. Chan, T. Pham, M. Hu, Y. X. Qin, A. Zettl, C. Carraro, M. A. Worsley and R. Maboudian, *Flatchem*, 2017, **5**, 1–8.
120 D. M. Guo, P. J. Cai, J. Sun, W. N. He, X. H. Wu, T. Zhang, X. Wang and X. T. Zhang, *Carbon*, 2016, **99**, 571–578.
121 A. Harley-Trochimczyk, T. Pham, J. Chang, E. Chen, M. A. Worsley, A. Zettl, W. Mickelson and R. Maboudian, *Adv. Funct. Mater.*, 2016, **26**, 433–439.
122 H. X. Chu, J. Hu, Z. J. Li, R. Y. Li, Y. Q. Yang and X. L. Sun, *Sens. Actuators, B*, 2019, **298**, 126866.
123 X. Ma, Y. Xie, Y. H. Yu, L. M. Lu, G. B. Liu, Y. F. Yu and C. Y. Hu, *J. Electroanal. Chem.*, 2018, **823**, 437–444.
124 X. L. Niu, X. Y. Li, W. Chen, X. B. Li, W. J. Weng, C. X. Yin, R. X. Dong, W. Sun and G. J. Li, *Mater. Sci. Eng., C*, 2018, **89**, 230–236.
125 Y. Chen, G. Z. Yang, B. Liu, H. Kong, Z. Xiong, L. Guo and G. Wei, *Chem. Eng. J.*, 2022, **430**, 132721.
126 J. T. Liu, X. Ge, X. X. Ye, G. Z. Wang, H. M. Zhang, H. J. Zhou, Y. X. Zhang and H. J. Zhao, *J. Mater. Chem. A*, 2016, **4**, 1970–1979.
127 S. Kabiri, D. N. H. Tran, S. Azari and D. Losic, *ACS Appl. Mater. Interfaces*, 2015, **7**, 11815–11823.
128 Q. L. Fang and B. L. Chen, *J. Mater. Chem. A*, 2014, **2**, 8941–8951.
129 F. P. Carvalho, *J. Environ. Radioact.*, 2018, **186**, 124–130.
130 N. L. Torad, M. Hu, M. Imura, M. Naito and Y. Yamauchi, *J. Mater. Chem.*, 2012, **22**, 18261–18267.
131 I. Lee, S. M. Kang, S. C. Jang, G. W. Lee, H. E. Shim, M. Rethinasabapathy, C. Roh and Y. S. Huh, *J. Mater. Chem. A*, 2019, **7**, 1737–1748.
132 J. B. Huo, G. C. Yu and J. L. Wang, *Sci. Total Environ.*, 2021, **761**, 143286.
133 K. Gupta, B. L. Yuan, C. Chen, N. Varnakavi and M. L. Fu, *Chem. Eng. J.*, 2019, **369**, 803–812.
134 Y. Li, H. J. He, Z. C. Liu, Z. E. Lai and Y. Wang, *J. Radioanal. Nucl. Chem.*, 2021, **328**, 289–298.
135 P. Song, M. L. Wang, J. Di, J. Xiong, S. R. Zhao and Z. Li, *ACS Appl. Nano Mater.*, 2020, **3**, 8176–8181.
136 S. C. Hou, X. Y. Wu, Y. Lv, W. Jia, J. X. Guo, L. X. Wang, F. L. Tong and D. Z. Jia, *Appl. Surf. Sci.*, 2020, **509**, 144818.
137 X. Q. Jiang, C. C. Ban, L. Li, J. D. Hao, Z. Chen, X. Y. Li, W. P. Chen and X. W. Liu, *Diamond Relat. Mater.*, 2021, **120**, 108649.
138 C. Y. Cai, Z. C. Wei, Y. Z. Huang and Y. Fu, *Chem. Eng. J.*, 2020, **421**, 127772.

139 A. Q. Sun, X. Hou and X. G. Hu, *Nano Energy*, 2020, **70**, 104511.
140 D. A. Yaseen and M. Scholz, *Int. J. Environ. Sci. Technol.*, 2019, **16**, 1193–1226.
141 C. Xiang, R. H. Guo, J. W. Lan, S. X. Jiang, C. Wang, Z. F. Du and C. Cheng, *J. Alloys Compd.*, 2018, **735**, 246–252.
142 D. Kweku, O. Bismark, A. Maxwell, K. Desmond, K. Danso, E. Oti-Mensah, A. Quachie and B. Adormaa, *J. Sci. Res. Rep.*, 2018, **17**, 1–9.
143 D. Camper, J. E. Bara, D. L. Gin and R. D. Noble, *Ind. Eng. Chem. Res.*, 2008, **47**, 8496–8498.
144 P. Ammendola, F. Raganati and R. Chirone, *Chem. Eng. J.*, 2017, **322**, 302–313.
145 M. Xu, S. J. Chen, D.-K. Seo and S. G. Deng, *Chem. Eng. J.*, 2019, **371**, 693–705.
146 N. Chouikhi, J. A. Cecilia, E. Vilarrasa-García, S. Besghaier, M. Chlendi, F. I. Franco Duro, E. Rodriguez Castellon and M. Bagane, *Minerals*, 2019, **9**, 514.
147 Y. Liu, M. H. Xiang and L. Hong, *RSC Adv.*, 2017, **7**, 6467–6473.
148 N. Hsan, P. K. Dutta, S. Kumar, R. Bera and N. Das, *Int. J. Biol. Macromol.*, 2019, **125**, 300–306.
149 D. Xia, H. Li, J. Mannering, P. Huang, X. R. Zheng, A. Kulak, D. Baker, D. Iruretagoyena and R. Menzel, *Adv. Funct. Mater.*, 2020, **30**, 2002788.
150 M. Zeeshan, K. Yalcin, F. E. Sarac Oztuna, U. Unal, S. Keskin and A. Uzun, *Carbon*, 2021, **171**, 79–87.
151 W. J. Wang, J. Motuzas, X. S. Zhao and J. C. Diniz da Costa, *ACS Appl. Mater. Interfaces*, 2019, **11**, 30391–30400.
152 C. Androulidakis, M. Kotsidi, G. Gorgolis, C. Pavlou, L. Sygellou, G. Paterakis, N. Koutroumanis and C. Galiotis, *Sci. Rep.*, 2021, **11**, 13548.
153 Z. N. Liu, K. L. Xu, P. She, S. Y. Yin, X. D. Zhu and H. Sun, *Chem. Sci.*, 2016, **7**, 1926–1932.
154 H. Hsu, C. Kuo, J. Jehng, C. T. Wei, C. F. Wen, J. H. Chen and L. C. Chen, *J. Environ. Chem. Eng.*, 2019, **7**, 103414.
155 T. Qiao, M. F. Zhao, G. L. Xiu and J. Z. Yu, *Sci. Total Environ.*, 2016, **557–558**, 386–394.
156 N. R. Martins and G. Carrilho da Graça, *Sustain. Cities Soc.*, 2018, **42**, 259–275.
157 K. Min, S. Kim and S. Kim, *Sci. Rep.*, 2018, **8**, 9598.
158 K. Y. Zhao, J. Y. Huang, J. J. Mao, Z. W. Bao, Z. Chen and Y. K. Lai, *Chem. Eng. J.*, 2020, **395**, 125086.
159 S. Y. Zhang, J. Sun, D. Hu, C. Xiao, Q. Q. Zhuo, J. J. Wang, C. X. Qin and L. X. Dai, *J. Mater. Chem. A*, 2018, **6**, 16139–16148.
160 J. J. Mao, Y. X. Tang, Y. D. Wang, J. Y. Huang, X. L. Dong, Z. Chen and Y. K. Lai, *iScience*, 2019, **16**, 133–144.
161 M. N. Chong, B. Jin, C. W. K. Chow and C. Saint, *Water Res.*, 2010, **44**, 2997–3027.
162 J. D. Hu, C. Chen, T. Hu, J. S. Li, H. Lu, Y. Zheng, X. G. Yang, C. X. Guo and C. M. Li, *J. Mater. Chem. A*, 2020, **8**, 19484–19492.
163 C. Chen, J. D. Hu, X. G. Yang, T. Y. Yang, J. F. Qu, C. X. Guo and C. M. Li, *ACS Appl. Mater. Interfaces*, 2021, **13**, 20162–20173.
164 X. Li, J. D. Hu, T. Y. Yang, X. G. Yang, J. F. Qu and C. M. Li, *Nano Energy*, 2022, **92**, 106714.
165 J. D. Hu, D. Y. Chen, N. J. Li, Q. F. Xu, H. Li, J. H. He and J. M. Lu, *Small*, 2018, **14**, 1800416.
166 R. Y. Zhang, W. C. Wan, D. W. Li, F. Dong and Y. Zhou, *Chin. J. Catal.*, 2017, **38**, 313–320.
167 L. Z. Wu, X. Y. Yang, T. Chen, Y. Li, Q. Meng, L. Zhu, W. K. Zhu, R. He and T. Duan, *Chem. Eng. J.*, 2022, **427**, 131773.
168 Z. Wang, H. X. Liu, Z. Lei, L. Q. Huang, T. Wu, S. Liu, G. Y. Ye, Y. X. Lu and X. K. Wang, *Chem. Eng. J.*, 2020, **402**, 126256.
169 L. Tang, C. T. Jia, Y. C. Xue, L. Li, A. Q. Wang, G. Xu, N. Liu and M. H. Wu, *Appl. Catal., B*, 2017, **219**, 241–248.
170 Y. H. Peng, A. A. Kashale, Y. K. Lai, F.-C. Hsu and I. W. P. Chen, *Chemosphere*, 2021, **274**, 129795.
171 Z. N. Xu, J. X. Jiang, Q. Q. Zhang, G. B. Chen, L. M. Zhou and L. Li, *J. Colloid Interface Sci.*, 2020, **563**, 131–138.
172 J. Y. Zhang, J. Y. Mei, S. S. Yi and X. X. Guan, *Appl. Surf. Sci.*, 2019, **492**, 808–817.
173 Q. W. Liang, S. Ploychompoo, J. D. Chen, T. T. Zhou and H. J. Luo, *Chem. Eng. J.*, 2020, **384**, 123256.
174 T. T. Xiong, Y. Ye, B. Luo, L. P. Shen, D. M. Wang, M. K. Fan and Z. J. Gong, *Ceram. Int.*, 2021, **47**, 14290–14300.
175 J. D. Hu, D. Y. Chen, N. J. Li, Q. F. Xu, H. Li, J. H. He and J. M. Lu, *Appl. Catal., B*, 2018, **236**, 45–52.
176 D. N. Liu, D. Y. Chen, N. Y. Li, Q. F. Xu, H. Li, J. H. He and J. M. Lu, *Appl. Catal., B*, 2019, **243**, 576–584.
177 H. Jung, K. M. Cho, K. H. Kim, H.-W. Yoo, A. Al-Saggaf, I. Gereige and H.-T. Jung, *ACS Sustainable Chem. Eng.*, 2018, **6**, 5718–5724.
178 Z. W. Tong, D. Yang, J. F. Shi, Y. H. Nan, Y. Y. Sun and Z. Y. Jiang, *ACS Appl. Mater. Interfaces*, 2015, **7**, 25693–25701.
179 V. K. Bajpai, S. Shukla, I. Khan, S. M. Kang, Y. Haldorai, K. M. Tripathi, S. Jung, L. Chen, T. Kim, Y. S. Huh and Y. K. Han, *ACS Appl. Mater. Interfaces*, 2019, **11**, 43949–43963.
180 M. J. Liu, X. W. Liu, P. Wang and X. Zhang, *Colloids Surf., A*, 2021, **626**, 126886.
181 Y. Q. Jiang, S. Chowdhury and R. Balasubramanian, *J. Environ. Chem. Eng.*, 2020, **8**, 104300.
182 A. Palika, A. Armanious, A. Rahimi, C. Medaglia, M. Gasbarri, S. Handschin, A. Rossi, M. O. Pohl, I. Busnadiego, C. Gübeli, R. B. Anjanappa, S. Bolisetty, M. Peydayesh, S. Stertz, B. G. Hale, C. Tapparel, F. Stellacci and R. Mezzenga, *Nat. Nanotechnol.*, 2021, **16**, 918–925.
183 M. Peydayesh and R. Mezzenga, *Nat. Commun.*, 2021, **12**, 3248.
184 K. Takahashi and Y. Tanaka, *Dalton Trans.*, 2016, **45**, 10497–10499.
185 R. Ramprasad, R. Batra, G. Pilania, A. Mannodi-Kanakkithodi and C. Kim, *npj Comput. Mater.*, 2017, **3**, 54.
186 S. Ramakrishna, T. Y. Zhang, W. C. Lu, Q. Qian, J. S. C. Low, J. H. R. Yune, D. Z. L. Tan, S. Bressan, S. Sanvito and S. R. Kalidindi, *J. Intell. Manuf.*, 2019, **30**, 2307–2326.

 